KeAi

CHINESE ROOTS
GLOBAL IMPACT

Contents lists available at ScienceDirect

Petroleum Science

journal homepage: www.keaipublishing.com/en/journals/petroleum-science



Original Paper

Diffraction classification imaging using coordinate attention enhanced DenseNet



Tong-Jie Sheng ^a, Jing-Tao Zhao ^{b, *}, Su-Ping Peng ^c, Zong-Nan Chen ^a, Jie Yang ^a

- ^a College of Geoscience and Survey Engineering, China University of Mining and Technology (Beijing), Beijing, 100083, China
- ^b Engineering Research Center of Groundwater Pollution Control and Remediation, Ministry of Education, College of Water Sciences, Beijing Normal University, Beijing, 100875, China
- ^c State Key Laboratory for Fine Exploration and Intelligent Development of Coal Resources, China University of Mining and Technology (Beijing), Beijing, 100083. China

ARTICLE INFO

Article history: Received 27 January 2024 Received in revised form 10 February 2025 Accepted 26 March 2025 Available online 28 March 2025

Edited by Meng-Jiao Zhou

Keywords:
Diffraction imaging
Diffraction classification
Azimuth-dip angle image matrix
Coordinate attention
DenseNet

ABSTRACT

In oil and gas exploration, small-scale karst cavities and faults are important targets. The former often serve as reservoir space for carbonate reservoirs, while the latter often provide migration pathways for oil and gas. Due to these differences, the classification and identification of karst cavities and faults are of great significance for reservoir development. Traditional seismic attributes and diffraction imaging techniques can effectively identify discontinuities in seismic images, but these techniques do not distinguish whether these discontinuities are karst cavities, faults, or other structures. It poses a challenge for seismic interpretation to accurately locate and classify karst cavities or faults within the seismic attribute maps and diffraction imaging profiles. In seismic data, the scattering waves are associated with small-scale scatters like karst cavities, while diffracted waves are seismic responses from discontinuous structures such as faults, reflector edges and fractures. In order to achieve classification and identification of small-scale karst cavities and faults in seismic images, we propose a diffraction classification imaging method which classifies diffracted and scattered waves in the azimuth-dip angle image matrix using a modified DenseNet, We introduce a coordinate attention module into DenseNet, enabling more precise extraction of dynamic and azimuthal features of diffracted and scattered waves in the azimuth-dip angle image matrix. Leveraging these extracted features, the modified DenseNet can produce reliable probabilities for diffracted/scattered waves, achieving high-accuracy automatic classification of cavities and faults based on diffraction imaging. The proposed method achieves 96% classification accuracy on the synthetic dataset. The field data experiment demonstrates that the proposed method can accurately classify small-scale faults and scatterers, further enhancing the resolution of diffraction imaging in complex geologic structures, and contributing to the localization of karstic fracture-cavern reservoirs. © 2025 The Authors. Publishing services by Elsevier B.V. on behalf of KeAi Communications Co. Ltd. This is an open access article under the CC BY license (http://creativecommons.org/licenses/by/4.0/).

1. Introduction

The important objective of seismic exploration is to obtain high-precision seismic images of subsurface geological structures (Li and Qu, 2022). With the development of oil and gas exploration, the imaging accuracy of small-scale geological structures is increasingly demanded. Traditional seismic exploration techniques based on reflected waves can effectively unveil large-scale continuous geological structures, but they are challenging to finely delineate small-scale exploration targets such as tiny faults, karst caves, and fractures which are related to oil and gas

reservoirs. Seismic diffraction is a key tool to establish super-resolution which provides rich information related to small-scale inhomogeneous geological bodies (Wang et al., 2022, 2023; Zhao et al., 2021). However, the amplitude of diffractions is extremely low, which makes strong reflections always mask the existence of diffractions (Klokov et al., 2010). In the conventional seismic processing flow, reflected waves are considered as the main signal and thereby enhanced, while diffracted waves are often considered as noise and thereby dismissed (Zakarewicz et al., 2024a). Due to the influence of strong reflected waves, the information of small-scale exploration targets may be ignored in seismic images. Removing strong reflections and enhancing diffractions are a necessary step to detect small-scale geologic discontinuities by diffraction imaging.

^{*} Corresponding author. E-mail address: diffzjt@163.com (J.-T. Zhao).

T.-J. Sheng, J.-T. Zhao, S.-P. Peng et al. Petroleum Science 22 (2025) 2353–2383

Given the crucial importance of detecting small-scale objects in seismic exploration, the investigation of diffraction separation and imaging has garnered significant interest among researchers. In view of dynamic and kinematic differences between diffractions and reflections, the singular value decomposition (SVD) (Chen et al., 2023; Jiang et al., 2022; Lin et al., 2020, 2021a, 2021b; Liu et al., 2025), plane wave destruction (PWD) filter (Fomel et al., 2007: Lin et al., 2022a: Taner et al., 2006: Yu et al., 2017: Bashir et al., 2024), common virtual source transform (Li et al., 2021), double sparse transforms (Chen et al., 2022a) and deep learning method (Kim et al., 2022; Lowney et al., 2021a; Sheng and Zhao, 2022; Sheng et al., 2023) have been proposed for separating diffractions and reflections in post-stack or common-offset domain. Zhang et al. (2024) exploited the conditional denoising diffusion probabilistic model to separate diffractions and reflections in common-offset domain. In the frequency-wavenumber domain, the energy distribution of diffractions is over a wide range of wavenumbers, while reflections are the opposite. Based on this difference in energy distribution. Lin et al. (2022b) used the geometry mode decomposition method to extract diffracted waves in the f-k domain. Chen et al. (2024) proposed a diffraction separation method based on curvelet transform, which applies high-pass and median cascaded filters to eliminate reflected waves in the curvelet domain. Wei et al. (2024) exploited the principal component analysis (PCA) method to separate diffractions and further describe distribution of deep cavern-type reservoirs based on the extracted diffractions. Li et al. (2024a) first used the median filter to remove strong linear reflections, and then exploited the f-k filter and the tau-p filter to further improve the proportion of diffraction in the separated wavefield. Klokov and Fomel (2012) exploited the PWD filter and the hybrid Radon transform to extract diffractions in migrated dip-angle gathers. Lin et al. (2023) first used the geometric mode decomposition method to extract the linear wavefield in migrated dip-angle gathers, and then employed the leastsquares Gaussian distribution fitting method to separate diffractions in linear wavefield. Sun et al. (2022) extracted diffractions for migrated dip-angle gathers based on convolutional neural network (CNN) and adaptive subtraction strategy. Markovic et al. (2023) used the self-supervised deep learning method to improve the signal-to-noise ratio (SNR) of diffractions. They designed a diffraction denoising autoencoder to improve the SNR of diffracted signals in synthetic seismic data, ground-penetrating radar data, and hard-rock seismic data. Sheng et al. (2024) proposed a twophase diffraction imaging method in migrated dip-angle gathers. In the first phase, the pattern operator is used to suppress the reflected waves outside the stationary point. In the second phase, the reflection energy attenuation function is used to further attenuate the reflected waves near the stationary point. Li et al. (2023a) achieved diffraction separation and imaging by combining shorttime singular spectrum analysis and least-squares reverse time migration method of plane waves. Li et al. (2024b) proposed a leastsquares diffraction imaging method combining variational mode decomposition and reverse time migration. Since the diffractions have low rank characteristics and the reflections have sparse characteristics in azimuth-dip angle domain, Zhao et al. (2020) used the low-rank matrix decomposition to separate diffractions in azimuth-dip angle domain. Zhao et al. (2019) proposed a shotdomain diffraction separation method which used a spacevarying media filter to remove reflections. Li et al. (2023b) calculated the local slopes of reflections and diffractions in shot gathers based on normal moveout velocity and ray parameters, and extend the PWD-based diffraction separation method to the prestack data domain.

Apart from diffraction separation, efforts have also been made to improve resolution through diffraction pattern recognition and

classification methods, de Figueiredo et al. (2013) employed the knearest neighbors (kNN) pattern recognition algorithm to detect diffractor points. Serfaty et al. (2017) used the PCA to extract the geometric features of different wavefields in the directional gathers and then trained a CNN based on these features to achieve automatic classification of reflectors and diffractors. Tschannen et al. (2020) constructed a large synthetic dataset and trained a CNN to identify scattering objects in migrated dip-angle gathers. Markovic et al. (2022) proposed a diffraction pattern recognition method using U-Net for ground-penetrating radar (GPR) data. Znak and Gajewski (2023) proposed a data-derived seismic event identification method, which identified edge diffractions in the data domain using wavefront curvature matrices. The main targets of diffraction imaging include diffracted wave and wavefield from subsurface small-scale scatterers or velocity perturbation with regard to the limited scale of the Fresnel radius in all directions (Landa and Keydar, 1998). The former is associated with faults, reflector edges, and fractures, while the latter is called scattered wave and typically arises from small-scale scattering objects such as karst cavities. Accurately identifying and classifying diffracted and scattered waves on a diffraction image can greatly assist in locating different small-scale geologic structures and further enhancing the resolution of seismic exploration. It holds significant importance in achieving precise characterization of oil and gas reservoirs. Existing diffraction classification methods are generally performed in the common-offset gathers or the migrated dip-angle gathers. In these gathers, diffracted and scattered waves exhibit similar kinematic characteristics. The primary distinction between them lies in their dynamic characteristics, specifically that diffracted waves demonstrate a polarity reversal property, while scattered waves do not. However, these methods often overlook the azimuthal differences between diffracted and scattered waves and can face challenges in distinguishing between the two in the presence of complex geologic structures.

In fact, the propagation of diffracted and scattered waves in three-dimensional media has an azimuth difference. Considering the azimuth information of seismic data will help to distinguish diffracted and scattered waves. Protasov et al. (2021) proposed three new seismic diffraction attributes based on the propagation behavior of diffractions in three-dimensional media to determine fractures' orientation and distinguish diffracted and scattered waves. These attributes make full use of the azimuth information of seismic data, and depict the fractured and cavernous geological features in wide azimuth seismic data well. Smirnov et al. (2021) used an ellipse to approximate the shape of diffraction in the dipazimuth angle gathers, and defined the major and minor axis ratio of the ellipse as fracture reliability factor to distinguish diffracted and scattered waves. This attribute takes into account the kinematic characteristics of diffraction and is helpful for the evaluation of fractured reservoirs. Zhao et al. (2020) introduced the azimuth-dip angle image matrix, in which the dynamic and azimuth differences between diffracted and scattered waves are preserved. Therefore, it is more suitable to distinguish between diffracted and scattered waves in the azimuth-dip angle image matrix.

In this study, we propose a novel method for classifying different geologic structures related to diffracted and scattered waves (e.g., faults and karst cavities) in the diffraction image. According to the azimuth and polarity differences between diffracted and scattered waves in the azimuth angle image matrix, we use a modified DenseNet with coordinate attention for classifying diffracted and scattered waves. We refer to this modified DenseNet as the diffraction classification network (DC-Net). After performing DC-Net classification, the diffracted and scattered wave probability image will be obtained to indicate the probability that each imaging

point is scattered wave or diffracted wave, respectively. Finally, we use these probabilities to multiply with diffraction image to obtain high-resolution diffractor and scatterer image. The paper is organized as follows. First, we present the dynamic and kinematic characteristics of diffracted and scattered waves in azimuth-dip angle image matrix. Second, the proposed diffraction classification imaging method is introduced, which includes DC-Net architecture and diffracted and scattered waves classification workflows. Third, the numerical experiment on 3D synthetic data and real data application confirm the availability of the proposed method. Finally, we give some discussion about proposed method.

2. Methodology

2.1. Kinematic and dynamic characteristics of diffracted and scattered waves in the azimuth dip-angle image matrix

The Kirchhoff migration collects the scattered energy and shifts the structures to their true positions on the seismic section (Üge and Kanlı, 2024). In the seismic exploration of subsurface oil and gas reservoirs, migrated seismic images serve as the foundation for structural interpretation and subsequent seismic inversion (Zhou, 2024; Li et al., 2025a). The 3D Kirchhoff time migration (Schneider, 1987; Schleicher et al., 2007) can be written as

$$\boldsymbol{M}(\boldsymbol{i}, \tau_I) = \iint \boldsymbol{W}(\boldsymbol{i}, \tau_I, \boldsymbol{s}, \boldsymbol{r}) \frac{\partial}{\partial t} \boldsymbol{D}(\boldsymbol{s}, \boldsymbol{r}, t_{SI} + t_{IR}) d\boldsymbol{s} d\boldsymbol{r},$$
 (1)

where $\mathbf{s} = (x_S, y_S)$, $\mathbf{r} = (x_R, y_R)$ represent the surface locations of the source S and the receiver R within the migration aperture, respectively. $\mathbf{i} = (x_I, y_I)$ is surface location of imaging point I. \mathbf{D} is seismic data and τ_I is migrated time at imaging point I. \mathbf{W} denotes amplitude weight. t_{SI} and t_{IR} respectively represent the one-way traveltime determined by the raypaths from source S to imaging point I and from imaging point I to receiver R, as shown in Fig. 1.

In practice, the discrete form of Eq. (1) is used to calculate the migration image **M** (Perez and Marfurt, 2007):

$$\boldsymbol{M}(\boldsymbol{i},\tau_{l}) = \sum_{\boldsymbol{s}} \sum_{\boldsymbol{r}} \boldsymbol{W}(\boldsymbol{i},\tau_{l},\boldsymbol{s},\boldsymbol{r}) \frac{\partial}{\partial t} \boldsymbol{D}(\boldsymbol{s},\boldsymbol{r},t_{SI} + t_{IR}), \tag{2}$$

Eq. (2) implies that Kirchhoff migration calculates the value of imaging point I by weighted summation of data collected from multiple positions within the migration aperture (Perez and Marfurt, 2008). In fact, the two-way raypath from source S to imaging point I and back to receiver R corresponds to a set of dip angle and azimuth angle (Cheng et al., 2012). Let \mathbf{q}_S and \mathbf{q}_R represent the ray slowness of the source and receiver legs, respectively. The \mathbf{n}_τ denotes the vertical downward unit vector in the τ direction. The dip angle θ corresponding to the given two-way raypath shown in Fig. 1 is defined as follows (Zhao et al., 2020):

$$\theta = \begin{cases} -\cos^{-1}\left(-\frac{(\boldsymbol{q}_{S} + \boldsymbol{q}_{R}) \cdot \boldsymbol{n}_{\tau}}{|\boldsymbol{q}_{S} + \boldsymbol{q}_{R}|}\right), & \boldsymbol{q}_{S} + \boldsymbol{q}_{R} \geq 0\\ \cos^{-1}\left(-\frac{(\boldsymbol{q}_{S} + \boldsymbol{q}_{R}) \cdot \boldsymbol{n}_{\tau}}{|\boldsymbol{q}_{S} + \boldsymbol{q}_{R}|}\right), & \boldsymbol{q}_{S} + \boldsymbol{q}_{R} < 0 \end{cases}$$
(3)

And the azimuth angle φ corresponding to the given two-way raypath is defined as (Cheng et al., 2011)

$$\varphi = \tan^{-1} \frac{2x_I - (x_S + x_R)}{2y_I - (y_S + y_R)}.$$
 (4)

Therefore, according to the correspondence between the given two-way raypath and a set of dip angle θ and azimuth angle φ , we can define a matrix m_l with dip and azimuth dimensions at the

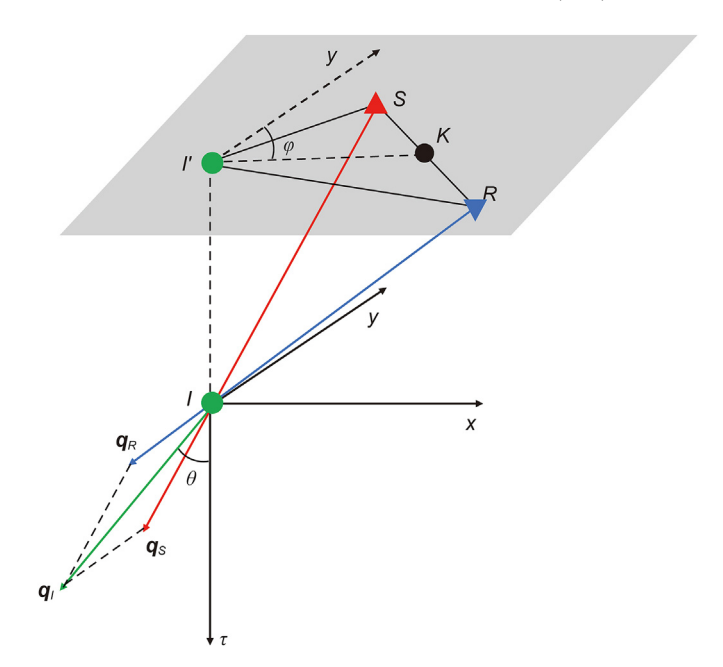


Fig. 1. The two-way raypath from source S to imaging point I and back to receiver R defines a set of azimuth angle φ and dip angle θ . \mathbf{q}_S and \mathbf{q}_R represent the ray slowness of the source and receiver legs, respectively. τ is migrated time. \mathbf{n}_τ denotes the vertical downward unit vector in the τ direction. The sum of the ray slowness \mathbf{q}_S and \mathbf{q}_R produces the illumination vector, $\mathbf{q}_I = \mathbf{q}_S + \mathbf{q}_R$. The dip angle θ corresponding to the given two-way raypath is defined as the angle between vector \mathbf{q}_I and vector \mathbf{n}_τ . K is the middle point of source S and receiver R. I' is the projection of the imaging point I onto the surface. The azimuth angle φ corresponding to the given two-way raypath is defined as the angle between I'K and Y axis.

imaging point I. In order to generate the azimuth-dip angle image matrix \mathbf{m}_I , the seismic data $\mathbf{D}(\mathbf{s}, \mathbf{r}, t_{SI}, t_{IR})$ should be migrated to the dip angle θ and azimuth angle φ in the matrix \mathbf{m}_I (Li et al., 2020). Eq. (2) is then modified as

$$\boldsymbol{m}_{I}(\varphi,\theta) = \sum_{(\boldsymbol{s},\boldsymbol{r}) \in \Omega} \boldsymbol{W}(\boldsymbol{i},\tau_{I},\boldsymbol{s},\boldsymbol{r}) \frac{\partial}{\partial t} \boldsymbol{D}(\boldsymbol{s},\boldsymbol{r},t_{SI} + t_{IR}), \tag{5}$$

where Ω is the set of two-way raypaths passing through the imaging point I with dip angle θ and azimuth angle φ . Summation of the azimuth-dip angle image matrix m_I over the azimuth angle φ and dip angle θ then produces a migration image according to the stationary phase principle (Bleistein et al., 2001):

$$\mathbf{M}(\mathbf{i}, \tau_I) = \sum_{\sigma} \sum_{\mu} \mathbf{m}_I(\varphi, \theta). \tag{6}$$

The energy-angle distributions in the azimuth-dip angle image matrix, which indicates the variation of seismic wavefield energy with azimuth angle and dip angle at the imaging point, are different for diffracted and scattered waves. We designed a simple 3D geologic model to show the dynamic and kinematic characteristics of diffracted and scattered waves in azimuth-dip angle image matrix. As shown in Fig. 2, the simple 3D geologic model contains a horizontal reflector and a scatterer with a radius of 5 m. The reflectivity of the horizontal reflector and the scatterer is set to 1 and 2, respectively. The velocity is set to 2000 m/s during modeling and migration.

We use the Kirchhoff migration algorithm to generate azimuth-dip angle image matrices. The scattered waves from the scatterer in the azimuth-dip angle image matrix are shown in Fig. 3(a). The scattered waves follow Huygens' principle and have their energy spread across wide ranges of azimuth and dip angle. The diffracted

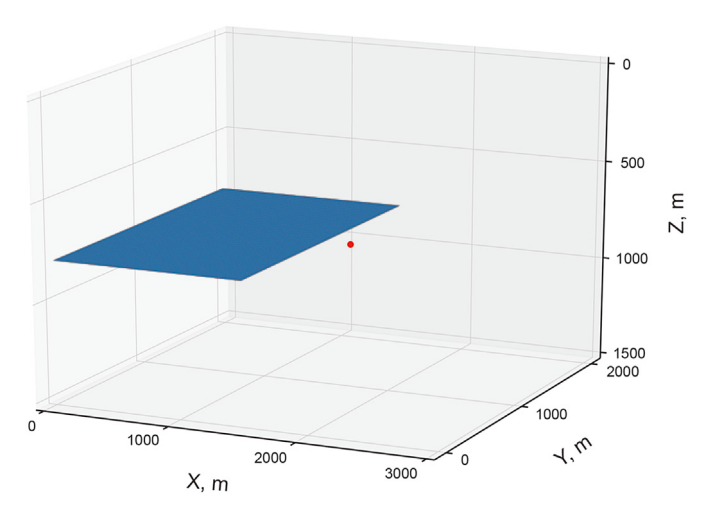


Fig. 2. The simple 3D geologic model contains a horizontal reflector and a scatterer. The scatterer with a radius of 5 m is located at x = 1500 m, y = 1000 m and z = 800 m. The reflectivity of scatterer and horizontal reflector are set to 2 and 1, respectively.

waves from the horizontal reflector's edge in the azimuth-dip angle image matrix are shown in Fig. 3(b). According to the geometrical theory of diffraction (Keller, 1962), the diffracted waves are limited by the azimuth angle, resulting in their energy is distributed in a narrow range of azimuth angle. What's more, the diffracted waves possess the polarity reversal property in the azimuth-dip angle image matrix. These dynamic and kinematic features provide a basis to classify diffracted and scattered waves in the azimuth-dip angle image matrix. However, it is worth noting that the presence of strong reflections, as indicated by the red arrow, obscures the diffracted waves in the azimuth-dip angle image matrix shown Fig. 3(b). It is difficult to observe the above-mentioned dynamic and kinematic characteristics of the diffracted waves in Fig. 3(b).

To mitigate the interference caused by reflections, we need to remove reflections before migration and then perform Kirchhoff migration algorithm on separated diffractions to produce the azimuth-dip image matrix. The PWD filter is a simple and powerful tool for separating diffraction and reflection. It assumes that reflection has better spatial coherence than diffraction, and therefore can be predicted by adjacent traces along the smooth local slope field, while diffraction is included in the prediction residuals (Wang et al., 2020). Its effectiveness has been widely recognized by researchers and has been successfully applied in many fields, often used as a comparison for new methods (Decker et al., 2015; Wang et al., 2020; Ford et al., 2021; Lowney et al., 2021b; Chen et al., 2022b, 2024; Li et al., 2023b; Sheng et al., 2024). It can eliminate strong reflections and highlight weak diffraction with minimal parameter adjustments (Zakarewicz et al., 2024b). This simplicity is beneficial for quickly processing large amounts of data (such as training dataset). Therefore, in this paper, we use the PWD method to extract diffraction. After removing reflections using PWD, the energy level of the wavefield in Fig. 3(c) has decreased from 10^{-8} (in Fig. 3(b)) to 10^{-10} , and the azimuth characteristic and polarity reversal property of diffracted waves masked by reflections can be clearly observed in Fig. 3(c). It demonstrates the necessity of removing reflections before classifying scattered and diffracted waves within the azimuth-dip angle image matrix.

2.2. Seismic wavefield classification in the diffraction image

In this work, we aim to classify the seismic wavefield in the diffraction image. There are three kinds of wavefield in the diffraction image: scattered wave, diffracted wave, and noise. The above problem can be regarded as an imaging point classification problem.

As mentioned above, each subsurface imaging point *I* has its own azimuth-dip angle image matrix m_l . Therefore, we can obtain the category of subsurface imaging point I by identifying the category of azimuth-dip angle image matrix m_i . By introducing the azimuth-dip angle image matrix, the imaging point classification task naturally becomes a 2D image matrix classification task. The CNN is a deep learning algorithm. CNNs have a large number of free parameters learned from the training data, which characterize certain patterns in the training data, establishing a non-linear mapping between the training data and the labels (Tschannen et al., 2020; Sheng and Zhao, 2022). And CNNs complete tasks on new data based on this non-linear mapping. CNNs have exhibited excellent performance in image recognition and classification tasks (Ke et al., 2017; Liu et al., 2017; Zhang et al., 2018; Wang et al., 2019), rendering them highly suitable for the classification of azimuth-dip angle image matrices.

For each subsurface imaging point, we use its azimuth-dip angle image matrix as the input to the network and make predictions to obtain the probabilities of each imaging point being a scattered wave, a diffracted wave, and noise, achieving pixel-level classification prediction. This classification process can be expressed as

$$\mathbf{p} = \text{Net}(\mathbf{m}_I),\tag{7}$$

where $\mathbf{p}=(p_0,p_1,p_2)$, such that $\sum_{i=0}^2 p_i=1$. p_0,p_1,p_2 represent the probabilities of noise, scattered wave and diffracted wave, respectively. Net(\cdot) represents the DC-Net architecture. \mathbf{m}_I is an azimuth-dip angle image matrix whose size is $M\times N$. M and N respectively represent the number of sampling points in the dip angle and azimuth angle.

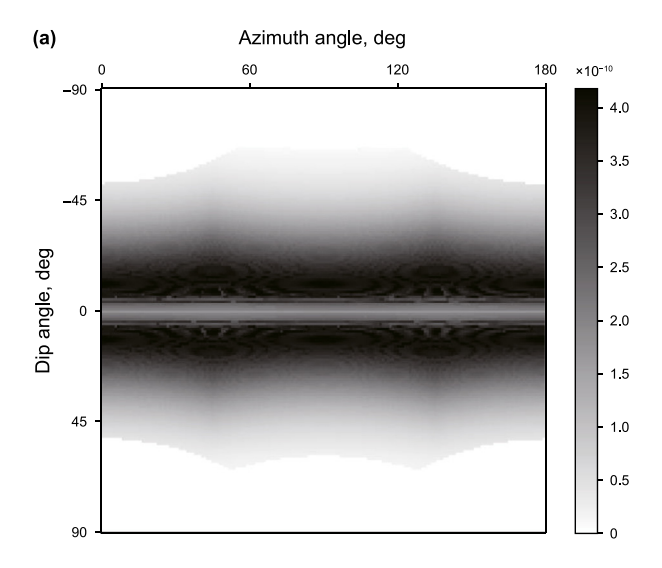
The flowchart of scattered and diffracted waves classification based on DC-Net is shown in Fig. 4. Its implementation steps are sketched as follows.

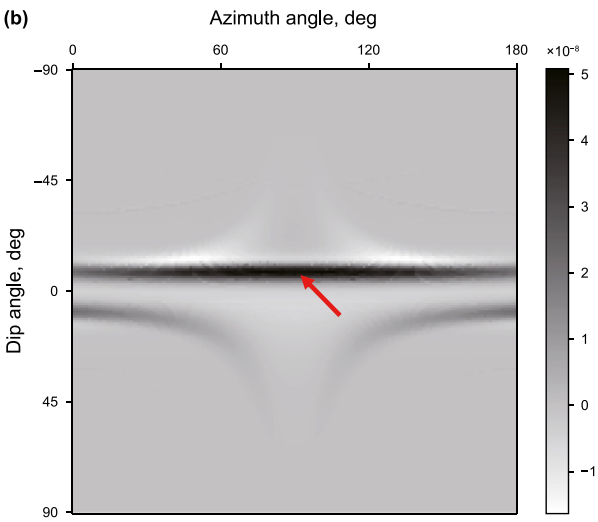
- 1) Apply the PWD method to 3D common-offset data to obtain 3D common-offset diffraction data.
- 2) Implement the Kirchhoff migration on 3D common-offset diffraction data to generate azimuth-dip angle image matrices.
- Input azimuth-dip angle image matrices to trained DC-Net and then perform DC-Net classification to gain diffracted and scattered wave probability.
- 4) Multiply the predicted diffracted and scattered wave probabilities with the diffraction image to obtain the high-resolution diffractor image and scatterer image.

2.3. DC-net architecture

It has been proven that short connections are beneficial in improving the performance of deep learning models in many deep learning studies (He et al., 2016). These short connections directly link early layers to later layers, allowing the feature maps from early layers to flow directly into the later layers. This alleviates vanishing gradients and network degradation. The DenseNet takes the concept of short connections to the extreme: it connects each layer to all subsequent layers through short connections (Huang et al., 2017), i.e., dense connection. Dense connections enable DenseNet to achieve high efficiency and accuracy in classification tasks. Hence, we utilize DenseNet to classify the diffracted and scattered waves in the azimuth-dip angle image matrix.

The DenseNet is primarily composed of a convolutional layer, dense blocks, transition layers, and a classification layer. When an





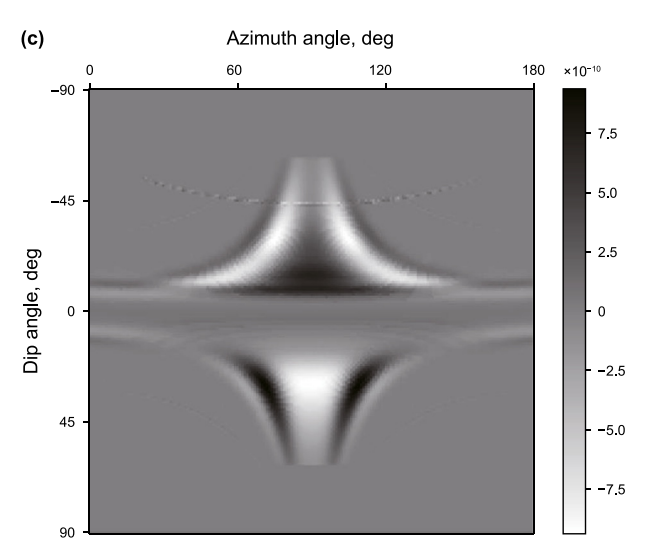


Fig. 3. The azimuth-dip angle image matrix. **(a)** Scattered waves at $x=1700\,\mathrm{m}$, $y=1000\,\mathrm{m}$ and $z=800\,\mathrm{m}$; **(b)** diffracted waves and reflections at $x=1700\,\mathrm{m}$, $y=1000\,\mathrm{m}$ and $z=800\,\mathrm{m}$; **(c)** separated diffracted waves at $x=1700\,\mathrm{m}$, $y=1000\,\mathrm{m}$ and $z=800\,\mathrm{m}$.

 $M \times N$ azimuth-dip angle image matrix is inputted into DenseNet, it is first processed by convolutional layer filtering. Let $H_d(\,\cdot\,)$ denotes a cascade of convolution, nonlinear activation function and batch normalization:

$$H_d(\cdot) = Conv^{d \times d} \{ReLU[BN(\cdot)]\},$$
 (8)

where d indexes the size of convolution kernel, $\operatorname{Conv}^{d \times d}(\cdot)$ is the $d \times d$ convolution, $\operatorname{ReLU}(\cdot) = \max\{0,\cdot\}$ is the rectified linear unit. $\operatorname{BN}(\cdot)$ is the batch normalization (loffe and Szegedy, 2015). The convolutional layer performs a cascade function $\operatorname{H}_7(\cdot)$ and 2×2 max pool on the azimuth-dip angle image matrix to generate feature maps, which are then inputted into the dense blocks.

The dense block is shown in Fig. 5(a). The dense block comprises K layers, where each layer performs composite non-linear transformation $G_k(\cdot)$. The composite non-linear transformation $G_k(\cdot)$ can be expressed as follows:

$$G_k(\cdot) = H_3(H_1(\cdot)), \tag{9}$$

where k indexes the layer.

Each layer within a dense block is connected to every other layer that follows. It means that any layer will receive the output feature maps of all the previous layers:

$$\boldsymbol{a}_k = G_k[Cat(\boldsymbol{a}_0, \boldsymbol{a}_1, ..., \boldsymbol{a}_{k-1})], \tag{10}$$

where \mathbf{a}_k represents the output feature map of the kth layer, $\mathrm{Cat}(\mathbf{a}_0, \mathbf{a}_1, ..., \mathbf{a}_{k-1})$ indicates the concatenation of the output feature maps in layers 0, 1, ..., k-1. The implementation of dense connection enables the features of diffracted and scattered waves extracted in each layer to be reused. It promotes the information flow between layers and alleviates the vanishing-gradient which makes the network easier to train and improves performance of the network on classification task.

The concatenation operation in Eq. (10) is unavailable when the operation of changing the size of feature maps, such as downsampling, is executed. The transition layer is introduced to connect two dense blocks to solve the above problems. The transition layer performs a composite non-linear transformation $T(\cdot)$ to change the size of feature maps:

$$T(\cdot) = AvgPool^{2\times 2}(H_1(\cdot)), \tag{11}$$

where $AvgPool^{2\times 2}(\cdot)$ is the 2 × 2 average pool.

In the azimuth-dip angle image matrix, besides the dynamic difference of polarity reversal between the diffracted wave and scattered wave, another important difference is the energy distribution difference between them in the azimuth angle direction. The coordinate attention module is helpful for network captures direction-aware and position-sensitive information about feature maps (Hou et al., 2021). We introduce the coordinate attention module before the classification layer to enhance the DenseNet's ability to extract features related to the energy distribution in the azimuth angle direction of diffracted and scattered waves. The coordinate attention module comprises two stages: coordinate information embedding and coordinate attention generation. The extraction of precise positional information and long-range dependencies along the spatial direction in coordinate information embedding involves the utilization of two pooling techniques:

$$\boldsymbol{a}_c^h = \frac{1}{N_a} \sum_{0 \le i < N_a} \boldsymbol{a}_c(h, i). \tag{12}$$

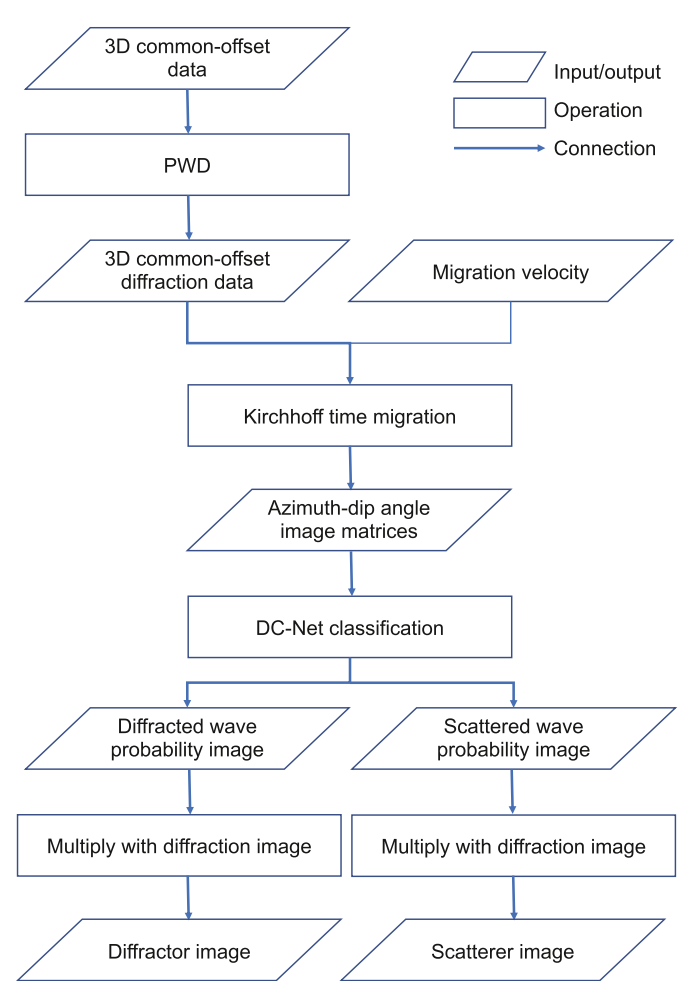


Fig. 4. Workflow of diffracted and scattered wave classification based on DC-Net.

$$\boldsymbol{a}_{c}^{w} = \frac{1}{M_{a}} \sum_{0 \le j < M_{a}} \boldsymbol{a}_{k,c}(j, w). \tag{13}$$

where \mathbf{a}_c is the c-th channel of feature map \mathbf{a} . M_a and N_a are the number of rows and columns of \mathbf{a} . h and w represent row and column indexes of \mathbf{a} .

The coordinate attention generation first concatenates the output of the coordinate information embedding and then input them into 1×1 shared convolution:

$$\mathbf{f} = \delta \left(\mathsf{Conv}^{1 \times 1} \left(\mathsf{Cat} \left(\mathbf{a}^h, \mathbf{a}^w \right) \right) \right). \tag{14}$$

where $\delta(\cdot)$ is non-linear activation function, \boldsymbol{a}^h and \boldsymbol{a}^w represent the data obtained after processing all channels of feature map \boldsymbol{a} through Eqs. (12) and (13), respectively.

The f is split into f^h and f^w along the spatial direction. The coordinate attention weights of feature map are generated by the following:

$$\mathbf{g}^h = \operatorname{Sigmoid}\left(\operatorname{Conv}^{1\times 1}\left(\mathbf{f}^h\right)\right).$$
 (15)

$$\mathbf{g}^{w} = \operatorname{Sigmoid}\left(\operatorname{Conv}^{1 \times 1}\left(\mathbf{f}^{w}\right)\right).$$
 (16)

where $Sigmoid(\cdot)$ is sigmoid function. Finally, the feature map \boldsymbol{b} adjusted by the coordinate attention module can be written as

$$\boldsymbol{b}_{c}(i,j) = \boldsymbol{a}_{c}(i,j) \times \boldsymbol{g}_{c}^{h}(i) \times \boldsymbol{g}_{c}^{w}(j). \tag{17}$$

where \mathbf{g}_c^h and \mathbf{g}_c^w represent \mathbf{g}^h and \mathbf{g}^w of the *c*-th channel, respectively. The \mathbf{b}_c is \mathbf{b} of the *c*-th channel.

After passing through a series of dense blocks, transformation layers, and coordinate attention module, the feature maps will be inputted into the classification layer to output the probabilities for different classes. The classification layer executes a batch normalization, linear layer and SoftMax on the final output feature map to

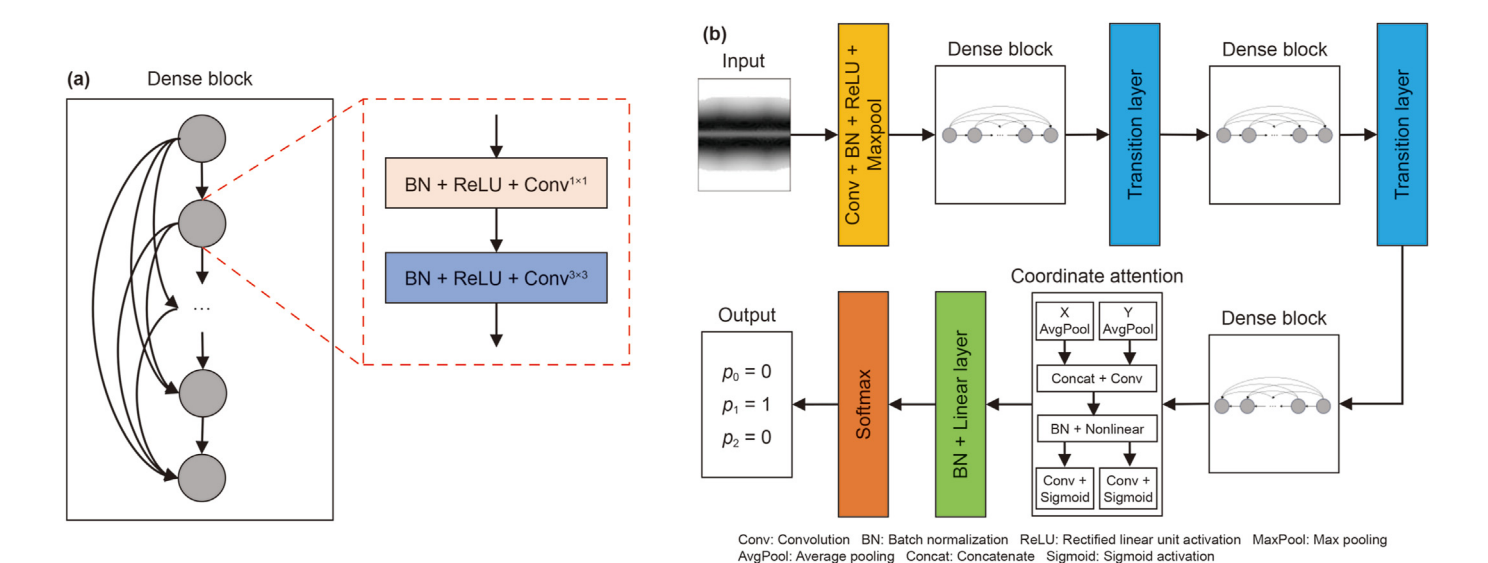


Fig. 5. The DC-Net architecture. (a) The dense block. (b) The DC-Net.

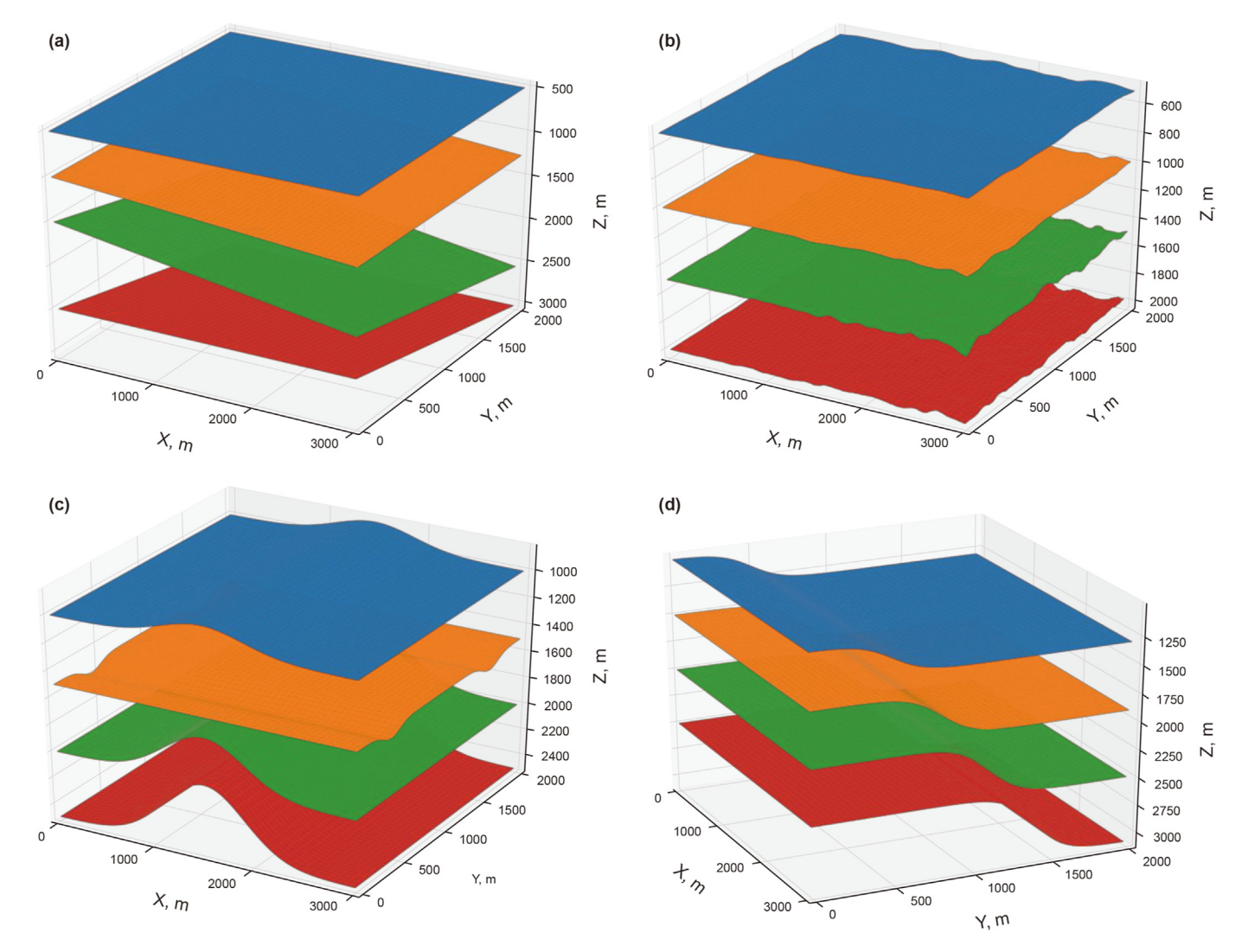


Fig. 6. Four types of basic geological models. (a) Inclined reflector model; (b) random curved reflector model; (c) Gaussian-type high slope reflector model; (d) S-type high slope reflector model.

obtain the probability vector \mathbf{p} . The DC-Net architecture is shown as Fig. 5(b).

3. Experiment

3.1. Dataset preparation

The effectiveness of the network is critically dependent on the quality of the training dataset (Goyes-Peñafiel et al., 2024; Li et al., 2024c). To obtain a deep learning model with high performance, it is widely recognized that a large and diverse training dataset is required (Park et al., 2019). We design four distinct types of three-dimensional geological models to construct a dataset of azimuth-dip angle image matrices. These four modes comprise the inclined reflector model, random curved reflector model, Gaussian-type high slope reflector model, and S-type high slope reflector model. The formula for constructing the inclined reflector model is as follows:

$$depth(l_x, l_y) = d_0 + l_x \cdot \tan \theta_x + l_y \cdot \tan \theta_y, \tag{18}$$

where l_x represents the position in the crossline direction of the model, l_y represents the position in the inline direction of the

model. depth(l_x , l_y) represents the function describing the variation of reflector depth with position. d_0 is the depth of the reflector at $l_x=0$ and $l_y=0$. θ_x represents the dip angle of the reflector along the crossline direction, while θ_y represents the dip angle of the reflector along the inline direction. The three-dimensional geological model constructed according to Eq. (18) is shown in Fig. 6(a).

In field data, reflectors often exhibit small undulations. We can simulate these small undulations in the reflectors using random functions and smooth functions. The random curved reflector model can be constructed using the following equation:

$$depth(l_x, l_y) = d_0 + l_x \cdot tan(smooth(rand(\theta_{xmin}, \theta_{xmax}))) + l_y \cdot tan(smooth(rand(\theta_{ymin}, \theta_{ymax}))),$$
 (19)

where rand(\cdot) represents the random number generator function, θ_{xmin} and θ_{xmax} represent the minimum and maximum values of the dip angles along the crossline direction generated by the random number generator. θ_{ymin} and θ_{ymax} represent the minimum and maximum values of the dip angle along the inline direction generated by the random number generator. smooth(\cdot) represents the smooth function used to smooth the randomly generated dip

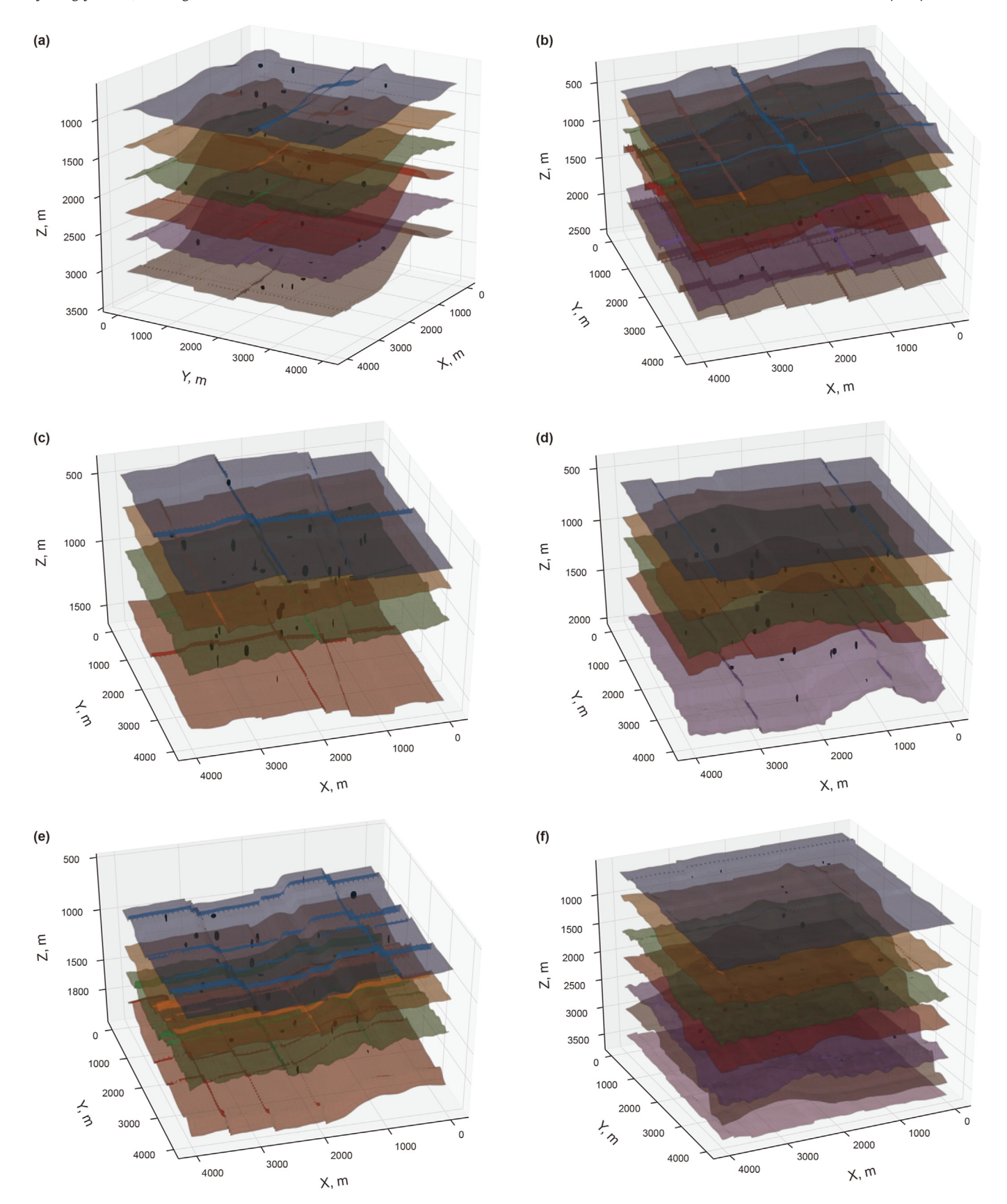


Fig. 7. Six 3D complex geological model examples used to generate training dataset.

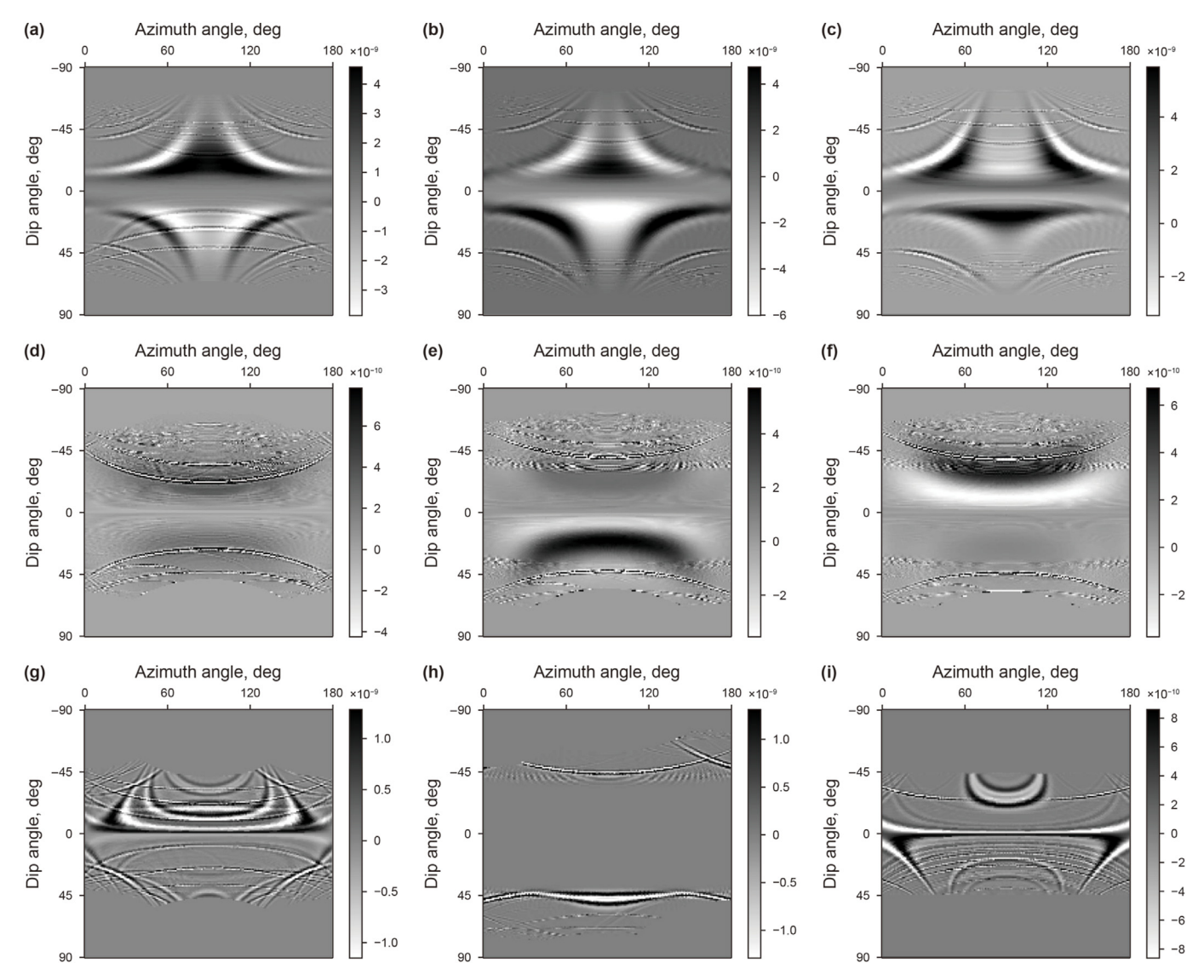


Fig. 8. Nine examples from the training dataset. The (a)—(c) show diffracted waves. The (d)—(f) show scattered waves. The (g)—(i) show residual reflections. There is some noise caused by the migration algorithm in the azimuth-dip angle image matrix.

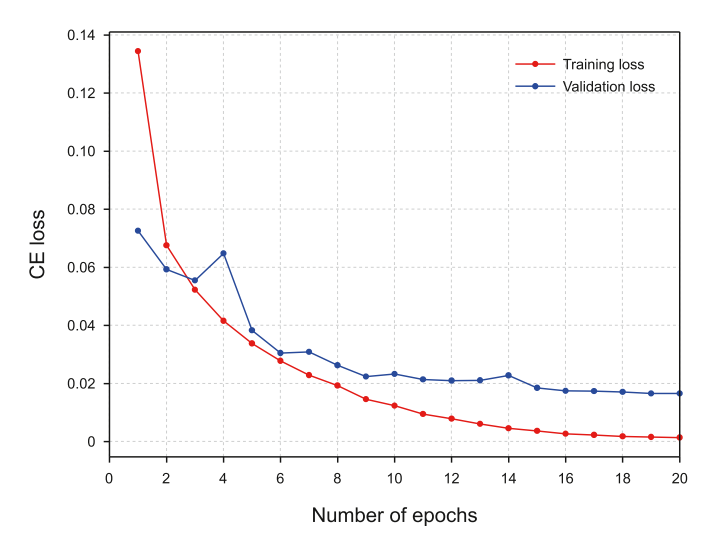


Fig. 9. The training and validation loss curves decreased steadily during the whole training process. The CE loss represents the cross entropy value defined in Eq. (22).

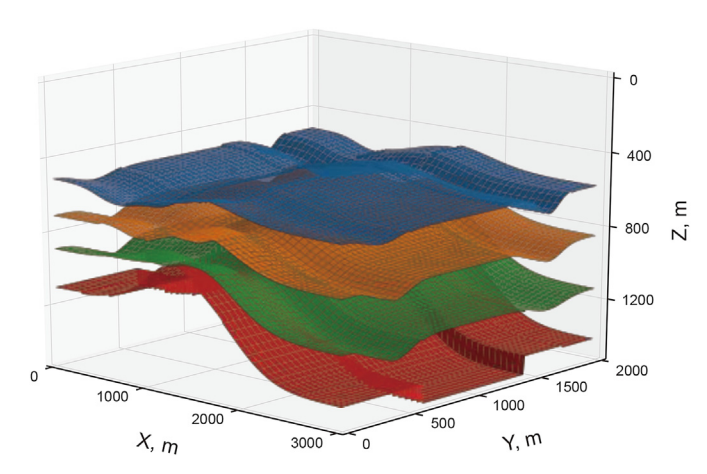


Fig. 10. The 3D geologic model, which contains curved reflectors, faults and scatterers.

angles. The three-dimensional geological model constructed according to Eq. (19) is shown in Fig. 6(b).

In addition to constant dip angles and small undulations, the reflection layer in practice may also have continuously changing high slope. We simulate continuously varying high slope reflectors using Gaussian and sigmoid functions. The Gaussian-type high slope reflector can be constructed using the following equation:

$$depth(l_x, l_y) = d_0 + \rho_{x1} \cdot e^{-\frac{(l_x - \mu_{x1})^2}{2\sigma_{x1}^2}} + \rho_{y1} \cdot e^{-\frac{(l_y - \mu_{y1})^2}{2\sigma_{y1}^2}},$$
(20)

where ρ_{x1} , μ_{x1} , σ_{x1} , ρ_{y1} , μ_{y1} and σ_{y1} are six parameters that control the shape of the Gaussian function. The three-dimensional geological model constructed according to Eq. (20) is shown in Fig. 6(c).

The high slope S-type reflector can be constructed using the following equation:

$$depth(l_x, l_y) = d_0 + \frac{\rho_{X2}}{1 + e^{-(l_x - \mu_{x2}) \cdot \sigma_{x2}}} + \frac{\rho_{y2}}{1 + e^{-(l_y - \mu_{y2}) \cdot \sigma_{y2}}}, \quad (21)$$

where ρ_{x2} , μ_{x2} , σ_{x2} , ρ_{y2} , μ_{y2} and σ_{y2} are six parameters that control the shape of the Sigmoid function. The three-dimensional geological model constructed according to Eq. (21) is shown in Fig. 6(d).

After constructing the reflector model, faults can be generated by dividing A into piecewise functions or adding displacement values in the depth direction. After adding faults to the reflector, we can introduce scatterers with different diameters into the model. These scatterers are used to generate scattered waves. More complex models can be obtained by combining these basic models. Based on the above process, training data can be generated in a batch manner by randomly generating reflector parameters, fault parameters, and scatterer parameters within specific ranges.

Finally, we generate 140 three-dimensional geological models whose size is 4000 m \times 4000 m \times 4000 m, which contain karstic caves of different scales, faults of different scales, and diverse large-scale reflection structures (including inclined strata of different dip angles, syncline, anticline and so on). The diameter of scatterers representing karstic caves is randomly set between 5 and 50 m, and these scatterers are randomly placed in the three-dimensional geological model to generate scattered waves of different shapes and amplitudes. Similarly, we randomly set the horizontal and vertical fault displacements between 5 and 50 m, and add different

fault displacements to the reflection structures to generate diffracted waves of different shapes and amplitudes. From our experiments, including more scatterers and faults in the geological model is helpful to train a better DC-Net, so we randomly set the number of faults in each three-dimensional geological model from 8 to 16 and the number of scatterers from 10 to 40. Six three-dimensional geological models from these 140 three-dimensional geological models are shown in Fig. 7.

After generating three-dimensional geological models in a batch manner, we establish a synthetic common-offset dataset by the 3D Kirchhoff modeling algorithm and implement the PWD method on the synthetic dataset to obtain a common-offset diffraction dataset. Subsequently, the azimuth-dip angle image matrices are generated using 3D Kirchhoff time migration algorithm on the common-offset diffraction dataset. A total of 210192 azimuth-dip angle image matrices are generated, we randomly divided the whole dataset into the training dataset and the validation dataset. Finally, the number of training dataset and validation dataset is 168591 and 41601, respectively. Nine azimuth-dip angle matrices from the training dataset are shown in Fig. 8.

3.2. Training DC-net

We train the DC-Net using the synthetic dataset. The training hyperparameters are set as follows: the batch size is set as 32 and the number of epochs is set as 20. We use the Adam algorithm to minimize loss function and update learnable parameters of DC-Net. We set the initial learning rate to 0.001 and use the cosine annealing algorithm to decay the learning rate in each epoch. During the training process, we use the cross entropy for the three classes to measure the difference between the output of the network and the expected output:

$$L_{\text{CE}} = -\frac{1}{B} \sum_{n=1}^{B} \sum_{c=0}^{2} \log \frac{\exp(p_{n,c})}{\sum_{i=0}^{2} \exp(p_{n,i})} \hat{p}_{n,c},$$
 (22)

where L_{CE} is cross entropy value, B is the number of training samples, $p_{n,c}$ and $\hat{p}_{n,c}$ respectively represent the network's output probability and actual probability for class c of the n-th training sample.

The training process costs a total of 13.29 h on a Dell precision tower 7910 workstation with one Quadro K6000 GPU and the

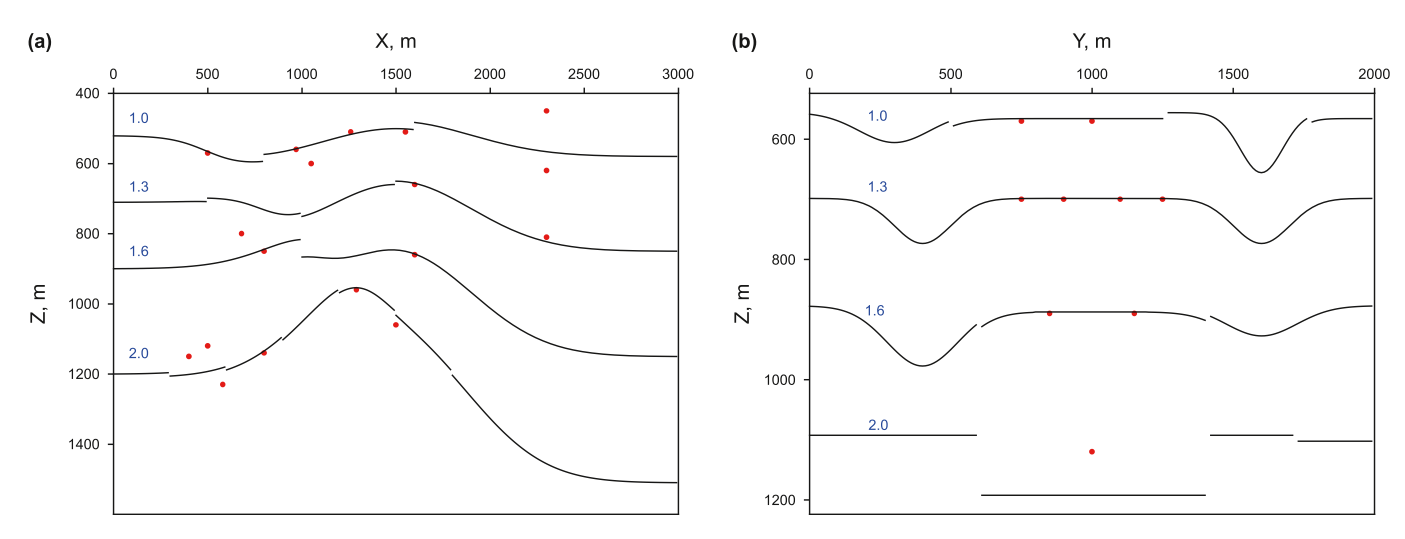


Fig. 11. (a) The XZ reflectivity section at y = 1000 m. (b) The YZ reflectivity section at x = 500 m. Black curves represent curved reflectors whose reflectivity is 1.0, 1.3, 1.6 and 2.0, respectively. Red dots represent scatterers with a radius of 5 m, and their reflectivity is set to 2.

CentOS7 operating system. The training and validation loss curves are shown in Fig. 9. The training and validation loss curves gradually converge steadily at the end of training.

3.3. Numerical examples

We meticulously design a 3D geologic model to test the effectiveness of the DC-Net. The 3D geologic model which contains curved reflectors, faults and scatterers is shown in Fig. 10. The reflectivity of the 3D geologic model is shown in the XZ section and YZ section in Fig. 11(a) and (b). The size of faults in the 3D geologic model is set to 10–100 m, and the radius of the scatterers is set to 5 m.

We generate common-offset data using 3D Kirchhoff modeling algorithm with a constant velocity of 2000 m/s and a 35 Hz Ricker wavelet. The common-offset data and the corresponding 3D Kirchhoff time migration are shown in Figs. 12 and 13, respectively. In Fig. 13, the reflections mask the existence of the scattered waves, especially area circled by red box, four scatterers are completely invisible due to their proximity to the reflector. Strong reflections will mask scattered and diffracted waves in the azimuth-dip angle image matrix, which is unfavorable to the classification of diffracted and scattered wave. We apply the PWD method to 3D commonoffset data to obtain 3D common-offset diffraction data. The common-offset diffraction data and the corresponding 3D Kirchhoff time migration are shown in Figs. 14 and 15, respectively. Compared to the 3D Kirchhoff time migration in Fig. 13, the diffraction image highlights faults and scatterers in Fig. 15. However, the distinction between diffracted and scattered waves is not obvious in the diffraction image due to the complexity of geological models. The diffracted waves indicated by the red arrows do not have obvious polarity reversal feature in Fig. 15, which makes it easy to be confused with scattered waves in the diffraction image. The residual reflections also cause a challenge in accurately locating scatterers and faults, for example, the diffracted waves indicated by the yellow arrows are covered by the residual reflections in Fig. 15, which are difficult to identify and locate. We generate the azimuth-

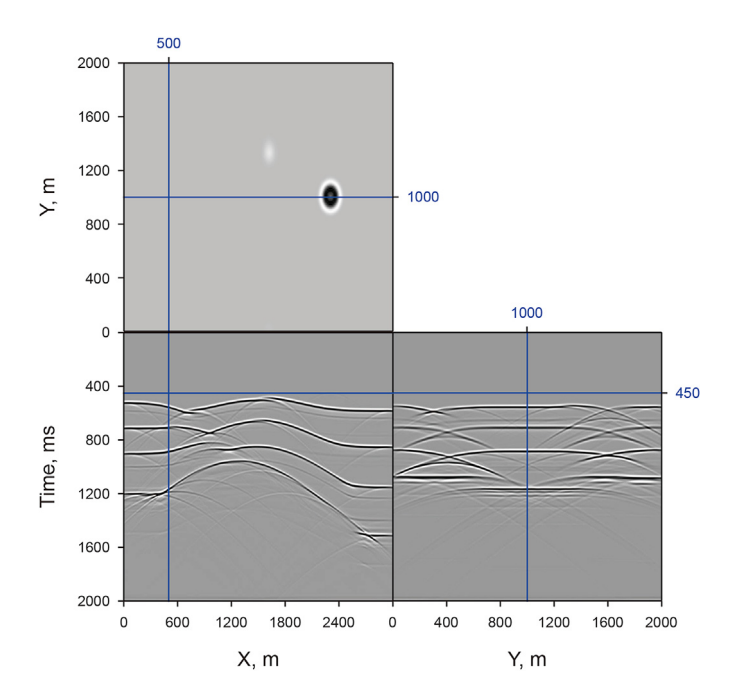


Fig. 12. The common-offset data of the 3D geologic model contains diffracted waves from the faults, scattered waves from the scatterers, and reflections from the curved reflectors.

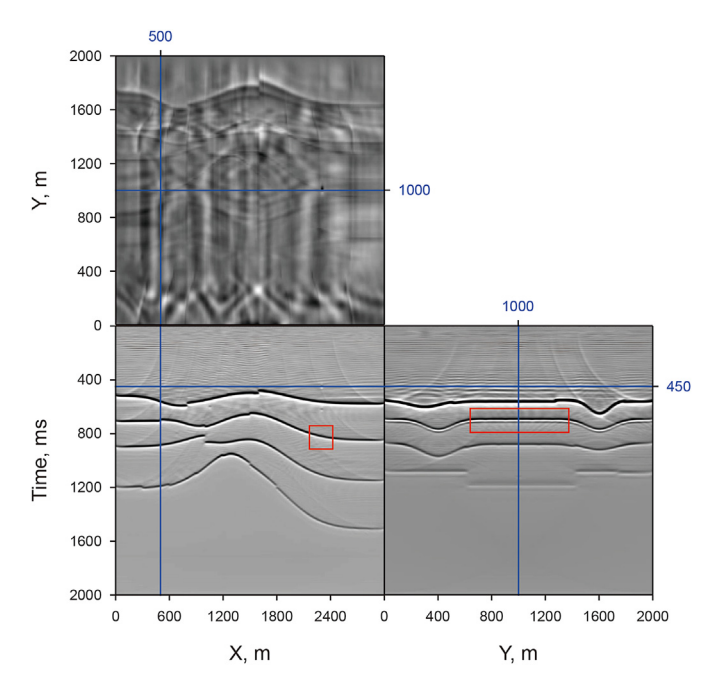


Fig. 13. The 3D Kirchhoff time migration of the 3D synthetic data. The 3D Kirchhoff time migration reveals curved reflectors and large-scale faults, while scatterers and small-scale faults are invisible due to the masking of reflections.

dip angle image matrix of each imaging point during the migration process, as shown in Fig. 16. When the subsurface structure is complex, the seismic wavefield also becomes complex, leading to the introduction of a large amount of migration noise in the azimuth-dip angle image matrix. Moreover, the complex wavefield makes it difficult for the PWD method to separate diffractions, resulting in residual reflections also present in the azimuth-dip angle image matrix. Compared to diffracted waves, the amplitude of scattered waves is weaker. This means that during the

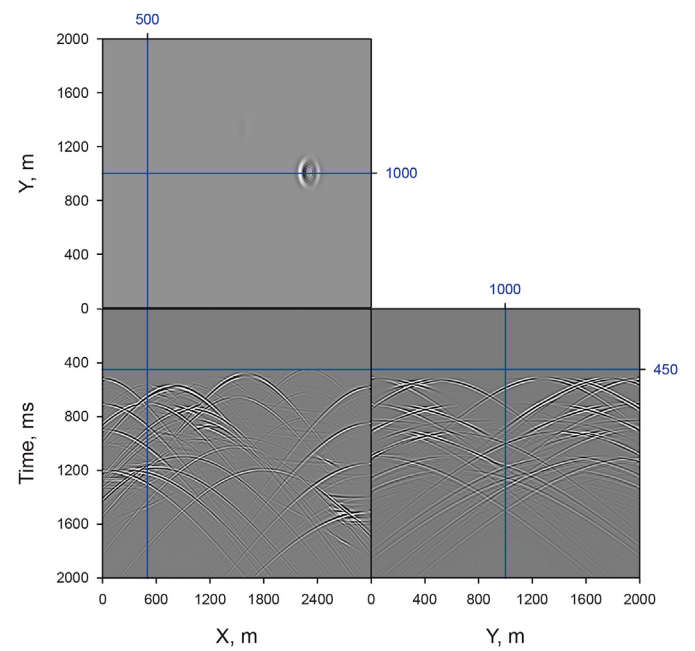


Fig. 14. Separated diffraction from the PWD method. The flat parts of the reflections are removed, but some of the high-slope parts of the reflection remain in the separated diffraction.

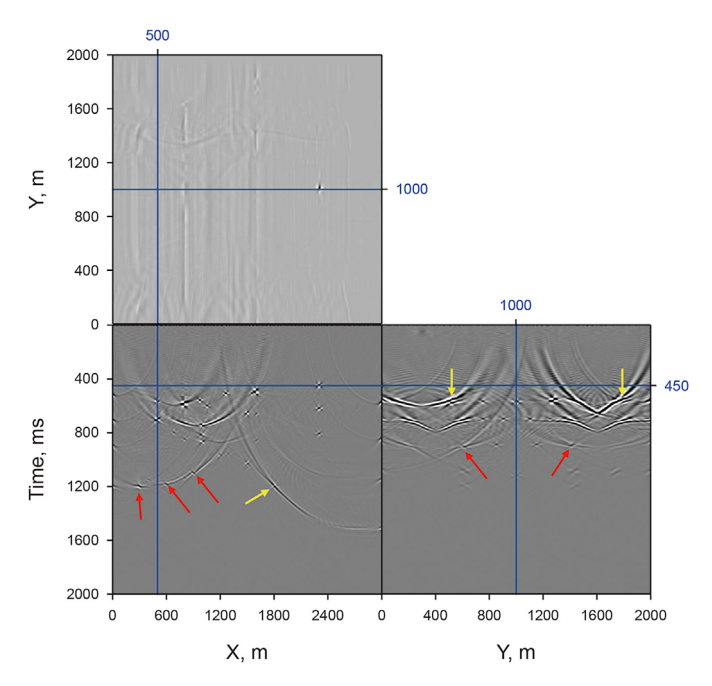


Fig. 15. The 3D diffraction image of the synthetic data. The small-scale faults and scatterers are highlighted. However, it is still difficult to distinguish the scattered and diffracted waves due to the complexity of the geological model and the residual reflections.

classification process, scattered waves are more affected by migration noise and residual reflections. The residual reflections and noise make the accurate classification of scattered and diffracted waves more challenging.

We use the DC-Net to classify the azimuth-dip angle image matrices of the diffraction data, and obtain diffracted and scattered wave probability images. We use evaluation metrics such as accuracy, precision, recall and F1-score in image segmentation tasks (Yang et al., 2024) to quantitatively evaluate the performance of DC-Net. The accuracy, precision, recall and F1-score of DC-Net on test dataset (generated from the 3D model shown in Fig. 8) are 96.03%, 88.16%, 54.76% and 62.71%. The diffracted and scattered wave probability images are shown in Fig. 17. The highlighted areas accurately indicate the positions of diffracted and scattered waves. However, as analyzed earlier, migration noise and residual reflections affect the classification results of scattered and diffracted waves. Some imaging points without scattered and diffracted waves are also considered to have a high probability of scattered or diffracted waves. The amplitude of these imaging points that do not have scattered and diffracted waves but have high probability values on the scattered or diffracted wave probability image may not be very strong in the diffraction image (due to the weakening of migration noise in the azimuth-dip angle image matrix after superposition along the dip and azimuth angles). In order to alleviate the interference of the noise and residual reflections, we multiply the diffracted and scattered wave probabilities as imaging point weights with the diffraction image to obtain the high-resolution diffractor and scatterer images. As shown in Fig. 18, the diffractor and scatterer images clearly reveal the positions of faults and scatterers. The faults masked by residual reflections (indicated by the yellow arrow) and without obvious polarity reversal characteristics (indicated by the red arrow) in the diffraction image are also clearly revealed on the diffractor image in Fig. 18(a). It demonstrates the effectiveness of the proposed method in locating and identifying faults and scatterers.

To further demonstrate the effectiveness of the proposed DC-

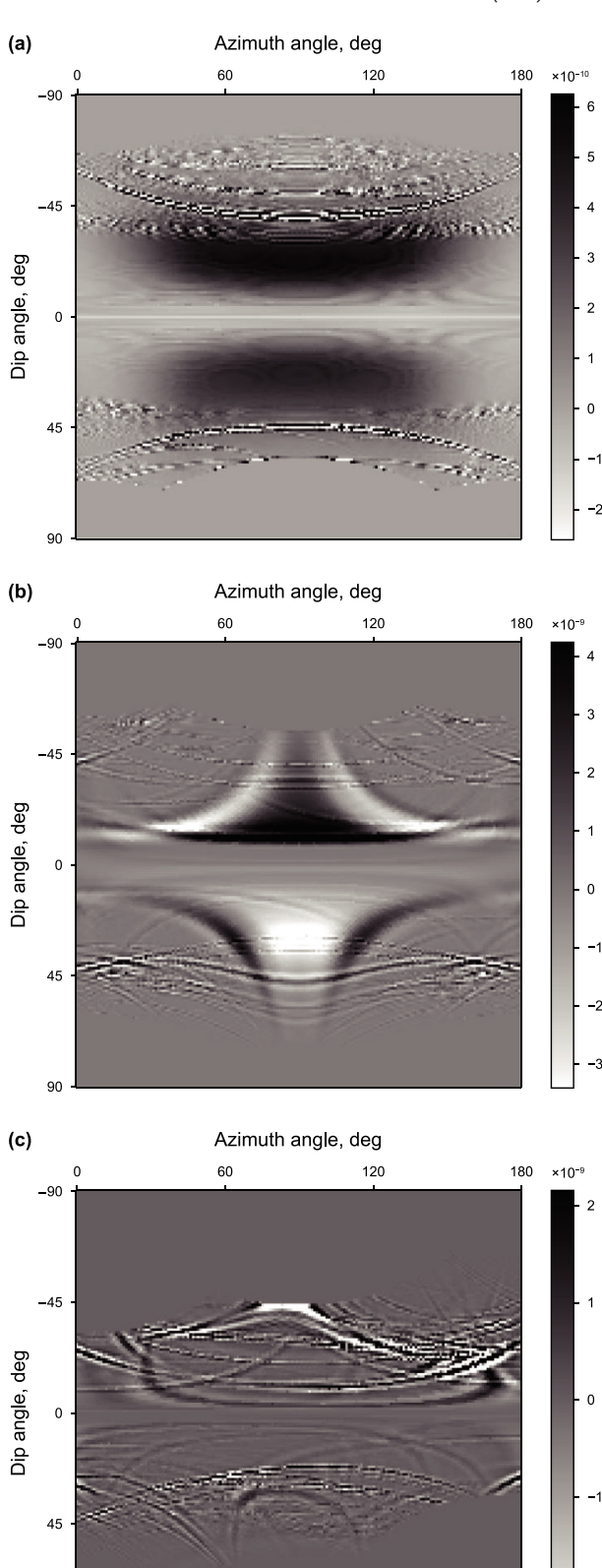


Fig. 16. The azimuth-dip angle image matrix of synthetic data. **(a)** Scattered wave at x = 2300 m, y = 1000 m, t = 450 ms; **(b)** diffracted wave at t = 800 m, t = 1000 m, t = 586 ms; **(c)** residual reflection at t = 500 m, t = 750 m, t = 790 ms.

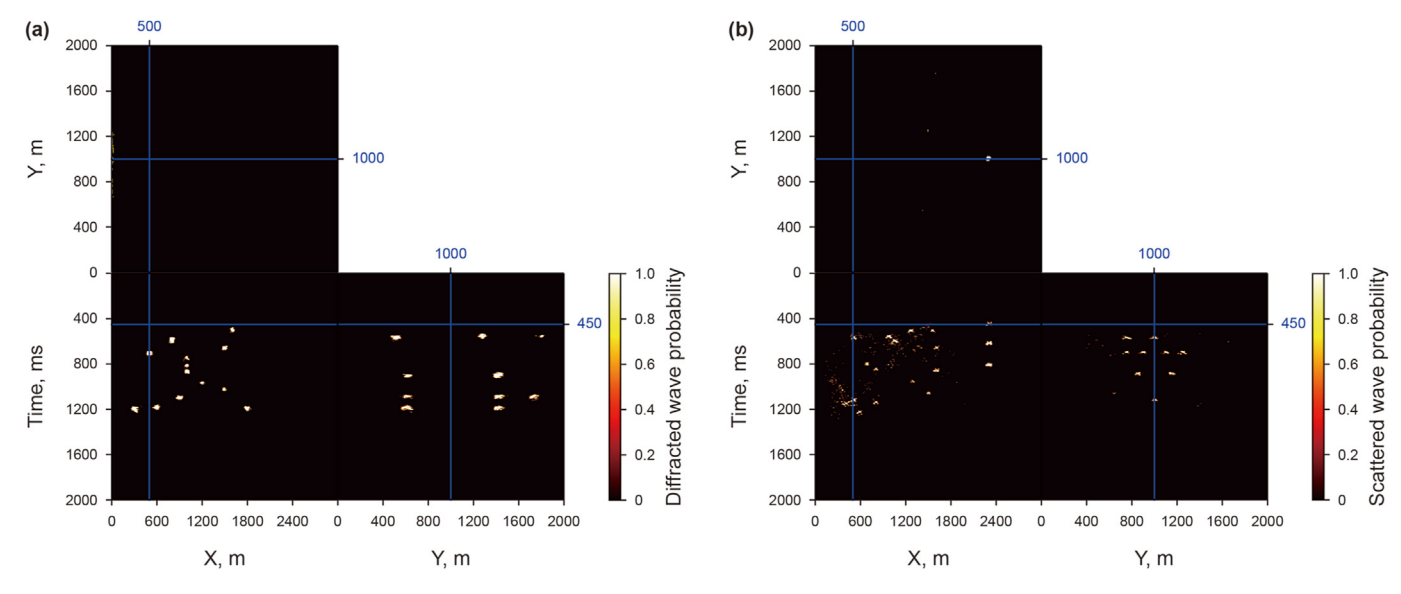


Fig. 17. The probability images. (a) The diffracted wave probability image. (b) The scattered wave probability image.

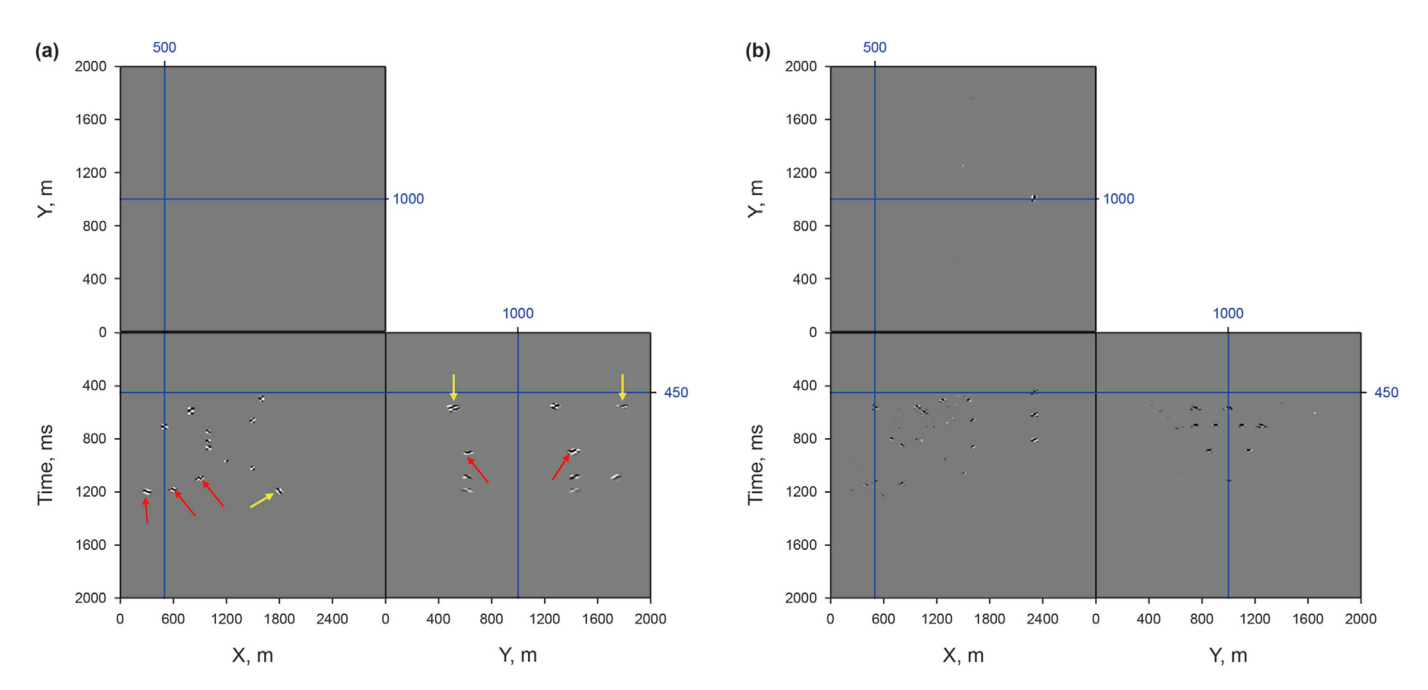


Fig. 18. The product images of diffraction image and probability image. (a) The diffractor image. (b) The scatterer image.

Net, we test and compare it with conventional the ResNet (He et al., 2016) and the DenseNet (Huang et al., 2017). We use the same training dataset to train ResNet and DenseNet. Table 1 presents the prediction performance of these networks on test data. The DC-Net receives the highest scores in accuracy and precision. The prediction results are shown in Fig. 19. These three networks effectively

Table 1Evaluation statistics of classification results of ResNet, DenseNet and DC-Net.

Evaluation,%	ResNet	DenseNet	DC-Net
Accuracy	95.64	95.59	96.03
Precision	87.79	80.87	88.16
Recall	51.49	58.12	54.76
F1-score	58.13	64.29	62.71

indicate the location of faults. There are differences among these three networks in predicting weak amplitude scatterers. As shown in Fig. 19(f), ResNet predicts poorly the scatterers indicated by the white arrows. DenseNet can effectively predict the position of certain scatterers, but there are false scatterers indicated by white arrows in Fig. 19(d). Compared to DenseNet and ResNet, DC-Net exhibits better scatterer prediction results in Fig. 19(b). We perform prediction using these three networks on one Quadro K6000 GPU to test imaging speed of these three networks. The time required by DC-Net, DenseNet, ResNet to predict one azimuth-dip angle image matrix is 36.39, 33.99 and 40.89 ms, respectively. Due to the introduction of the coordinate attention module, the imaging speed of DC-Net is slightly lower than that of DenseNet. This sacrifice in imaging speed is worthwhile because coordinate attention effectively improves prediction precision (compare

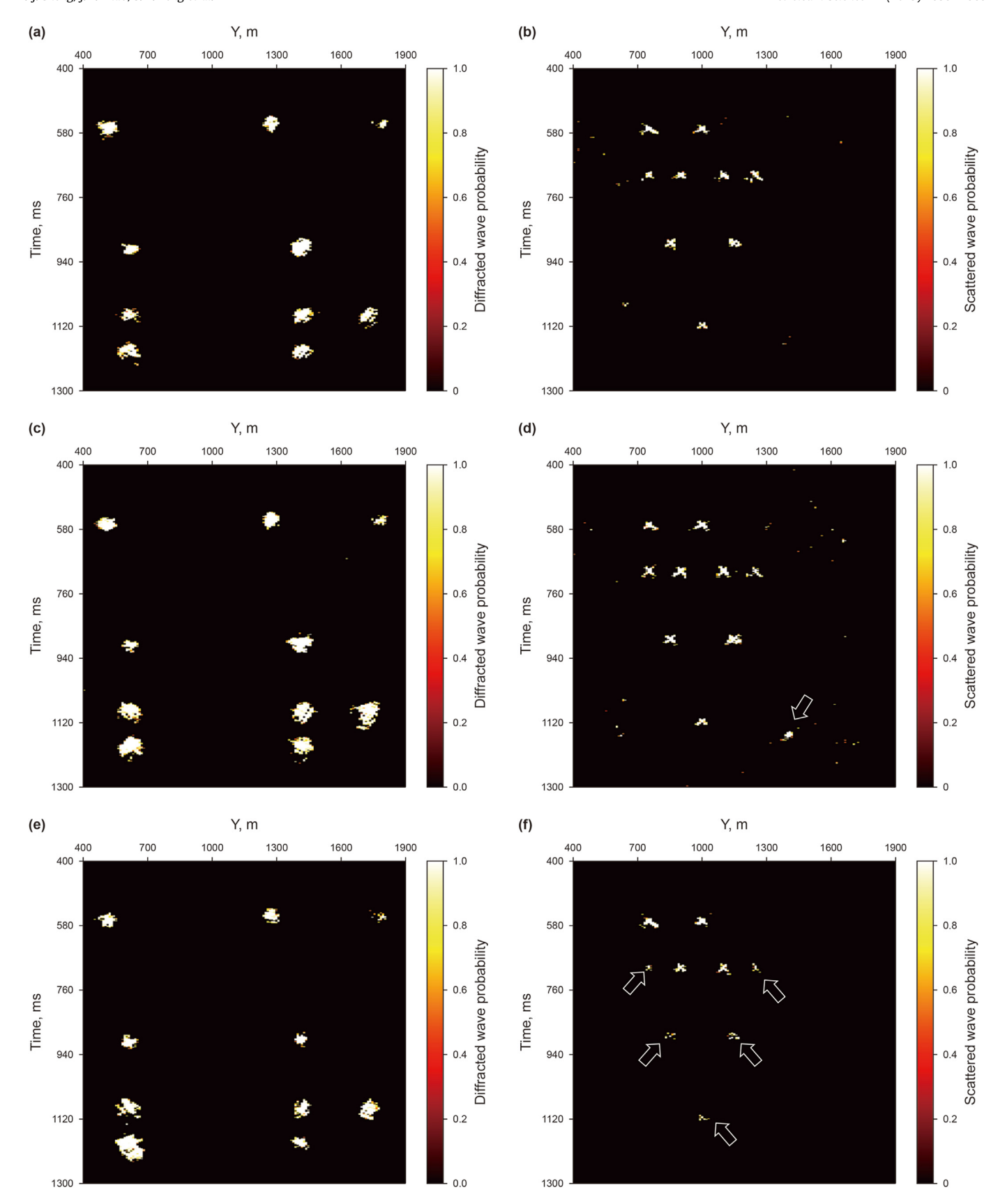


Fig. 19. The prediction results of DC-Net, DenseNet and ResNet. The (a) and (b) are the diffracted and scattered wave probability images predicted by DC-Net, respectively. The (c) and (d) are the diffracted and scattered wave probability images predicted by DenseNet, respectively. The (e) and (f) are the diffracted and scattered wave probability image predicted by ResNet, respectively.

Fig. 19(b) and (d)). The comparison experiments validate the advantages of the proposed DC-Net over other conventional networks in the diffraction classification imaging task.

Accurately distinguishing diffracted and scattered waves in the diffraction image is a key to identify and locate faults and scatterers. There may be no obvious dynamic differences between diffracted and scattered waves in the diffraction image when subsurface structures are complex. Meanwhile, the reflections remaining in the diffraction image also further improve the difficulty of distinguishing diffracted and scattered waves. This 3D geologic model application proves that our proposed classification method can effectively classify diffracted and scattered waves, primarily owed to DC-Net's great performance in extracting distinctive characteristics of diffracted and scattered waves in the azimuth-dip angle image matrix.

3.4. Field data application

We further verify the effectiveness of the proposed method on a 3D real post-stack dataset from North China. The research area where the 3D real post-stack dataset is located is developed with Ordovician limestone karst fracture-cavern reservoirs. These reservoirs exhibit several distinct characteristics, including small scale, strong heterogeneity, and deep burial depth. These characteristics make it difficult to accurately depict the location of the reservoir with reflection imaging. In contrast, diffraction imaging, which focuses on imaging small-scale elements, can provide high-resolution information about subsurface heterogeneity. It is helpful to detect small-scale caves and faults in the research area, and to realize the fine characterization and accurate identification of karst fracture-cavern reservoirs in the research area.

The 3D real post-stack dataset is shown in Fig. 20(a) and the corresponding Kirchhoff time migration is displayed in Fig. 20(b). We use the red dots and dashed lines to indicate the location of the well A and B. The location of the target layer is indicated by a blue curve. Well A exhibits low yield, whereas well B has produced industrial gas flow, suggesting the presence of reservoirs in its proximity. The resolution of the reflection image is low, and only

large-scale reflectors can be clearly observed in the reflection image. Although some parts of the reflector can be observed to be bent in the reflection image, these bends may be caused by small-scale geological bodies near the reflector or by reflector fluctuations. The reflection image cannot provide enough information to accurately locate small-scale geological bodies. The separated diffraction using the PWD method and the corresponding Kirchhoff time migration are displayed in Fig. 21. Compared with the reflection image, the diffraction image provides more detailed information about small-scale geological bodies. However, distinguishing faults and scatterers still remains difficult in the diffraction image. This makes it challenging to accurately identify karst fracture-cavern reservoirs within the research area.

The synthetic dataset generated under ideal conditions often cannot effectively represent all the features of field data. Especially, in addition to the differences in waveforms and amplitudes, there is "background noise" in the real data that is not present in the synthetic data. It is worth noting that the real data in Fig. 20(a) are the data that can be directly used for migration after denoising and other pre-processing. This background noise is the background value that still exists in the data after denoising and other preprocessing. This background noise is related to factors such as the survey and geological conditions of the study area, so it is different for different real data. It is difficult to simulate this background noise in synthetic data that can cover all cases. As a data-driven method, the DC-Net trained with synthetic dataset may not be able to effectively classify diffracted and scattered waves in real dataset because of the difference between synthetic dataset and real dataset. Training a new DC-Net from scratch is time-consuming and tedious. Transfer learning is helpful to solve this problem and it has been performed in diffraction separation (Kim et al., 2022), fault detection (Cunha et al., 2020) and other seismic data processing based on deep learning. Transfer learning can be achieved in various ways, with the most common method being the use of pre-trained models. We used the DC-Net trained on synthetic data as the pre-trained model. The pre-trained model has learned the general features of scattered and diffracted waves in azimuth-dip angle image matrices from a large-scale synthetic dataset. The

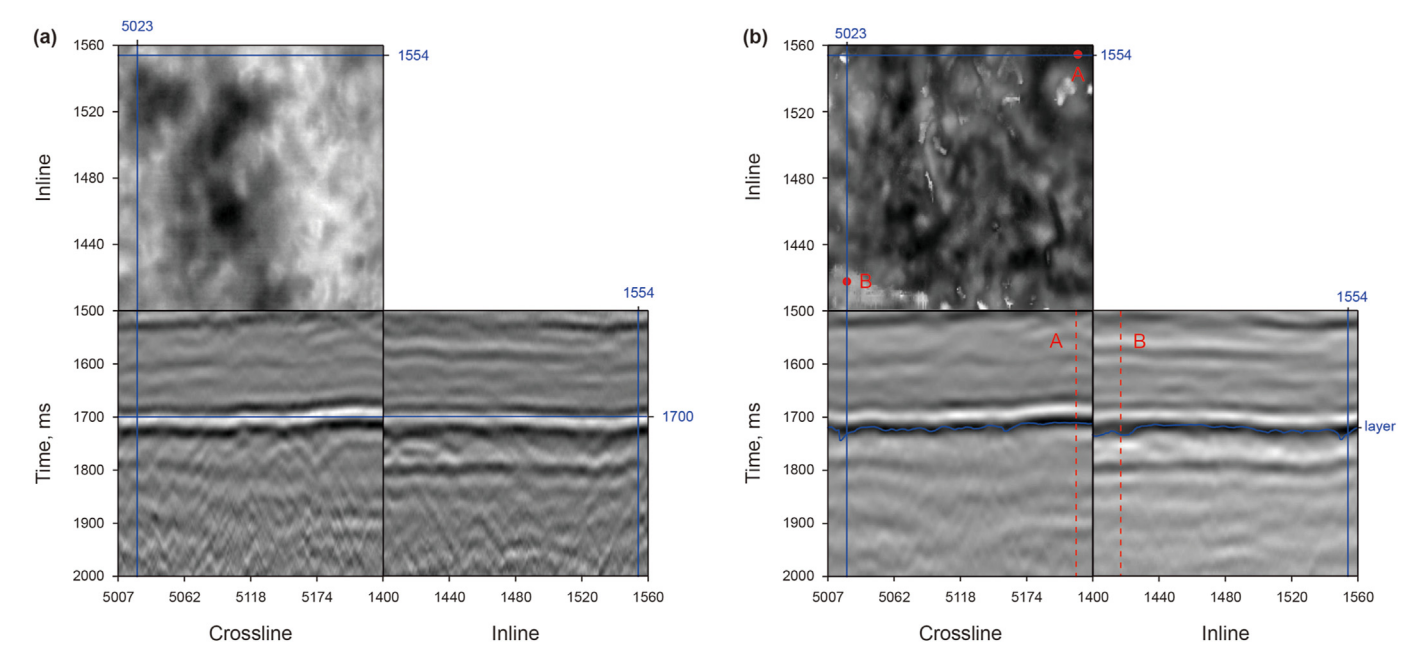


Fig. 20. (a) The 3D real post-stack data. (b) The reflection image. The information provided by the low resolution of reflection imaging is not enough to accurately locate the small-scale geological body.

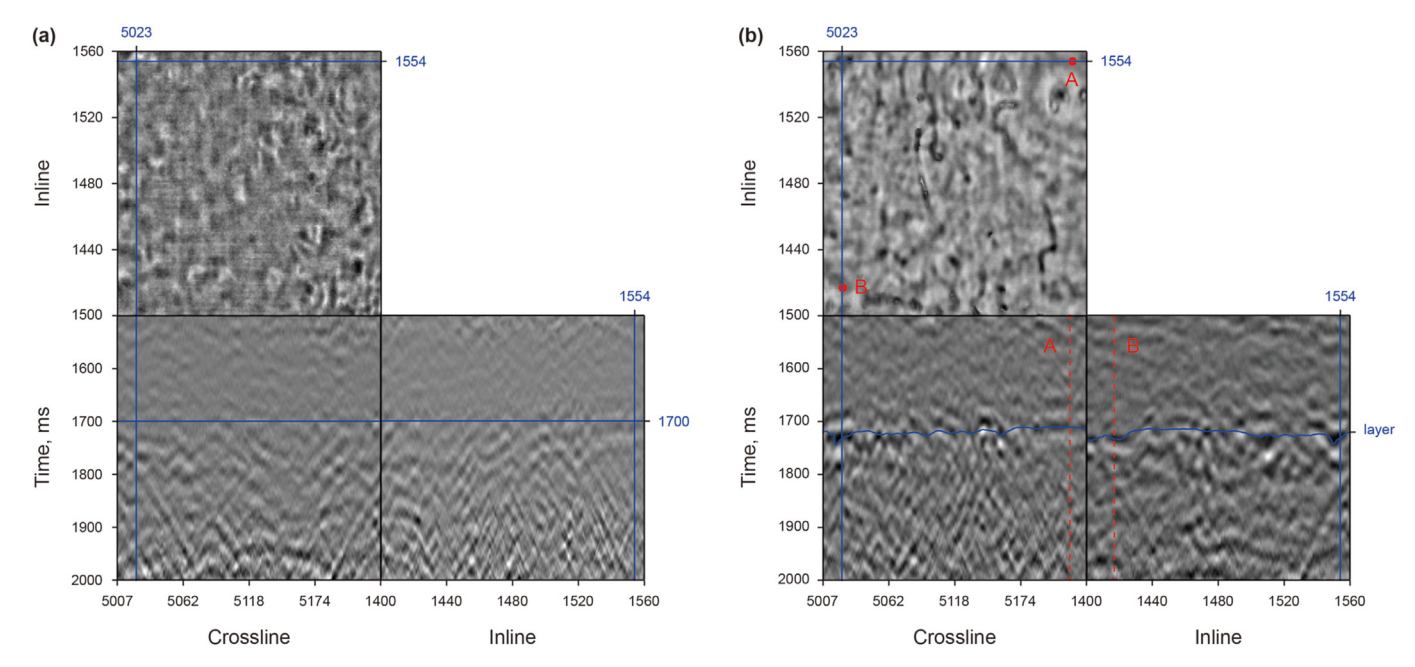


Fig. 21. (a) The separated diffraction using the PWD method. (b) The diffraction image. The diffraction image provides more detailed information about small-scale geological bodies, but faults and scatterers are still difficult to distinguish.

pre-trained model will be used as the initial model to fine tune parameters on additional small-scale training dataset to avoid a time-consuming retraining. We select 9 lines of data from the real dataset to generate azimuth-dip angle image matrices and make labels by manually marking the diffracted and scattered waves in azimuth-dip angle image matrices. These azimuth-dip angle image matrices will be used as the additional training dataset of DC-Net for processing the field data. Note that the additional training data does not include the subsequent field test data. To prevent overfitting, the initial learning rate should be small in transfer learning (Kim et al., 2022). We set the initial learning rate to 0.0001 and applied all of the strategies described previously.

DC-Net classification results of diffraction image are shown in Fig. 22. Compared with the diffraction image, diffracted and scattered wave probability images provide a more detailed description. Scatterer and diffractor images can be obtained by multiplying scattered and diffracted wave probability images with the diffraction image, as shown in Fig. 23. The scatterer image reveals the existence of scatterers near well B, indicating that there is a high possibility of karst fracture-cavern reservoirs near well B. These findings align with the observation of industrial gas flow at well B. The scatterer and diffractor images show that there are no scatterers and faults near well A, which indicates that there may be no karst fracture-cavern reservoirs near well A. This may be the reason for the low production of well A.

Seismic attribute analysis has proved to be a very effective technique for interpreting subsurface geological features and it has been widely used in industry (Ishak et al., 2018; Dell et al., 2020; Yang et al., 2023; Li and Li, 2024). We introduce a comparison between the seismic coherency attribute and the proposed method to demonstrate the effectiveness of the proposed method. The seismic coherency attribute of the field data in Fig. 20(b) is shown in Fig. 24(a). The seismic coherency attribute reveals many large-scale faults. However, due to the influence of strong reflections, the resolution of small-scale scatterers is not high in Fig. 24. Moreover, the seismic coherency attribute mainly enhances the discontinuity features in the image and does not differentiate between discontinuities caused by faults and discontinuities caused by scatterers.

In contrast to the seismic coherency attribute, the proposed method achieves the automatic classification of scatterers and faults in the diffraction image. It reveals effectively small-scale geological features hidden in the background of strong reflections and provides a more detailed portrayal of small-scale scatterers and faults.

Carbonate karst fracture-cavern reservoirs account for a considerable proportion of the reservoirs discovered worldwide and harbor enormous exploration and development potential (Decker et al., 2015; Li et al., 2016). The carbonate karst fracturecavern reservoirs contain various types of reservoir space, including caves and fractures (Li et al., 2016). Due to large differences in reservoir space, diverse development strategies are required for various types of carbonate fracture-cavity reservoirs. Therefore, it is necessary to distinguish geological structures related to reservoirs, such as caves and fractures. In seismic imaging, the caves correspond to scattered waves, while the fractures correspond to diffracted waves (Smirnov et al., 2021). The proposed method combines diffraction imaging and deep learning techniques to achieve the automatic classification imaging of scattered and diffracted waves, which alleviates the dependence of smallscale structures interpretation on manual experience to a certain extent. It has the potential to distinguish between caves and fractures in carbonate karst fracture-cavern reservoirs, which is conducive to enhancing the development and utilization of carbonate karst fracture-cavern reservoirs. The method can be integrated into current workflows. The proposed classification imaging workflow (Fig. 4) is based on diffraction imaging and acts on seismic data that can be directly used for migration. Thus, the classification imaging workflow (Fig. 4) can be inserted between data preprocessing and reflection imaging in the current workflows. The method can be naturally combined with conventional seismic attribute techniques to enhance the efficiency of reservoir development, i.e., the seismic attribute technique is used to portray large-scale structures and the proposed method is used to supplement the detailed information of small-scale structures.

The field data application illustrates that the proposed diffraction classification imaging method can further provide more

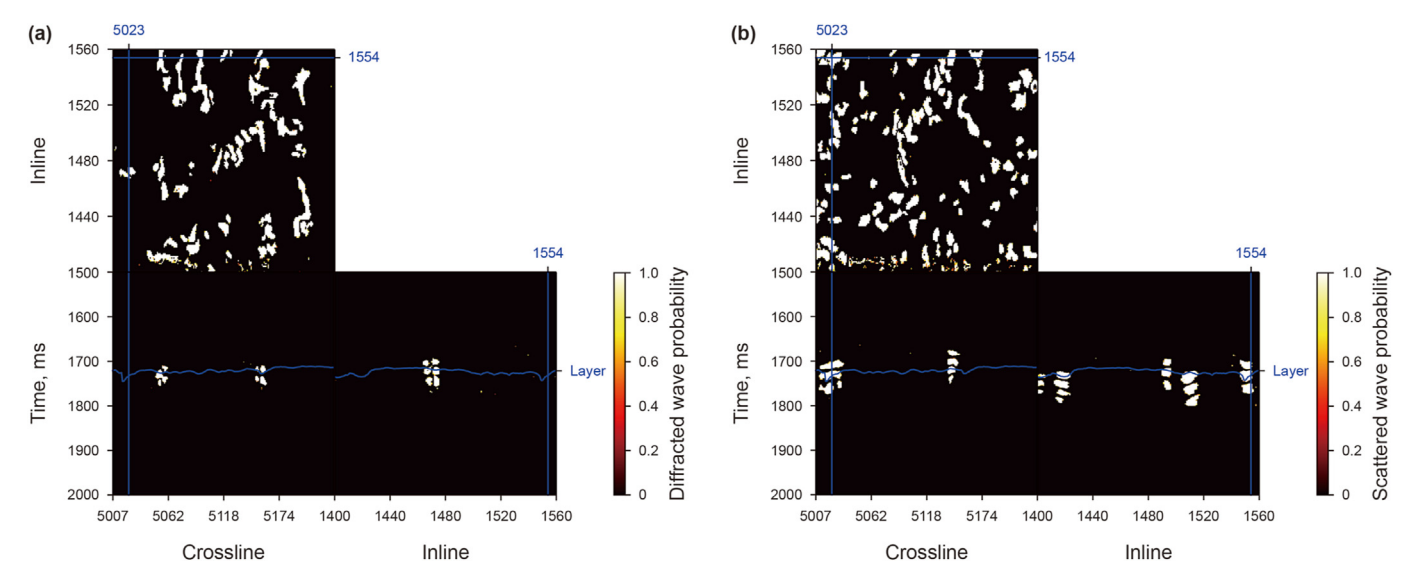


Fig. 22. The probability images. (a) The diffracted wave probability image; (b) the scattered wave probability image.

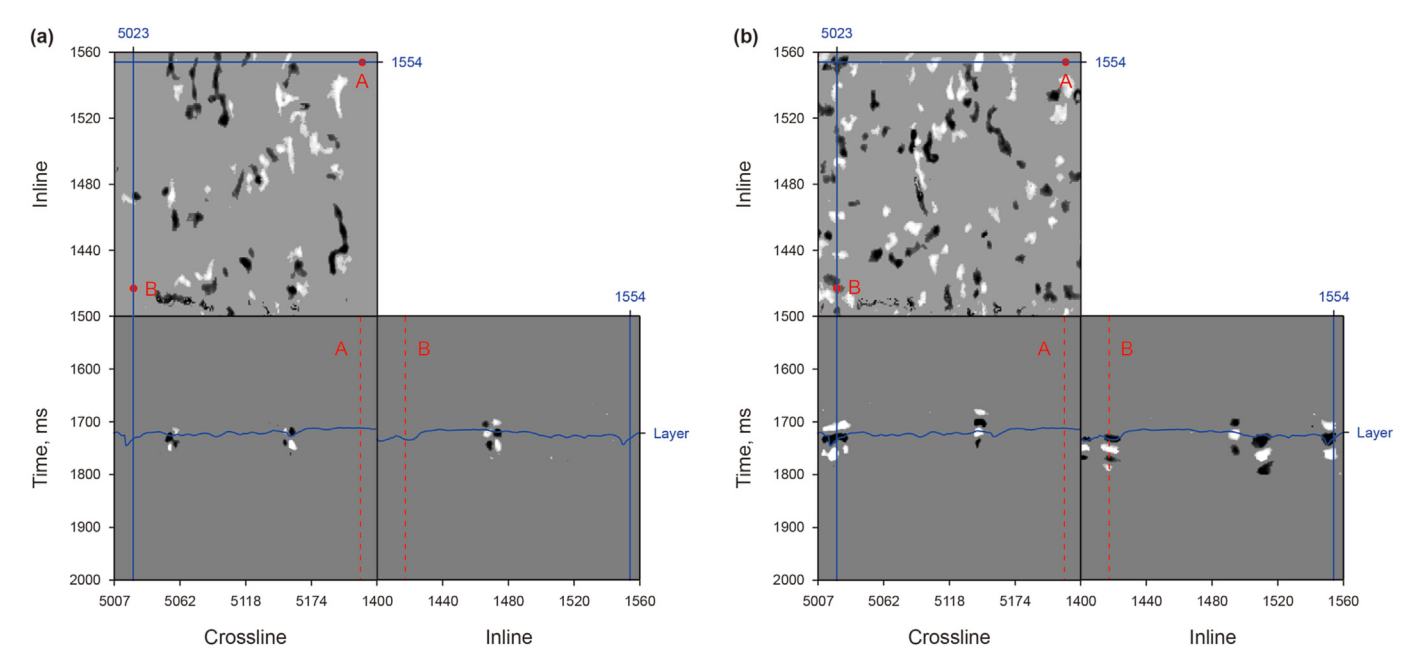


Fig. 23. The product images of the diffraction image and the probability images of real data. (a) The diffractor image. (b) The scatterer image. The scatterers near well B reveal the existence of reservoirs. The absence of faults and scatterers near well A suggests that it may be a low production well.

accurate and detailed characterization of scatterers and faults on the basis of the diffraction image, which improves the resolution of the diffraction image and is helpful for the exploration of karst fracture-cavern reservoirs.

4. Discussion

The DC-Net classifies diffracted and scattered waves according to their dynamic and kinematic characteristics in azimuth-dip angle image matrices. Errors in migration velocity can result in defocusing and distortion of scatterers and diffractors in migration images (Liu et al., 2024; Li et al., 2025b). These errors also affect the dynamic and kinematic characteristics of diffracted and scattered waves in azimuth-dip angle image matrices, so it may affect the classification results of the network. We test the impact of

migration velocity errors on the performance of the DC-Net trained by synthetic training dataset. The diffraction images with 2% and 5% errors in migration velocity are shown in Fig. 25. When the migration velocity is higher or lower than accurate migration velocity, distinct arcuate features can be observed in the diffraction images of faults and scatterers, while the energy of scattered and diffracted waves cannot be accurately focused at the true positions of scatterers and faults. This implies that migration velocity errors can affect both dynamic and kinematic characteristics of the azimuth-dip angle image matrices. The diffracted wave and scattered wave probability images at x = 500 m with inaccurate migration velocity are shown in Fig. 26. For 2% errors in migration velocity, the DC-Net can accurately classify the diffracted waves in Fig. 26(a) and (c), but the classification results of scattered waves are obviously affected in Fig. 26(b) and (d). When the errors are

T.-J. Sheng, J.-T. Zhao, S.-P. Peng et al. Petroleum Science 22 (2025) 2353—2383

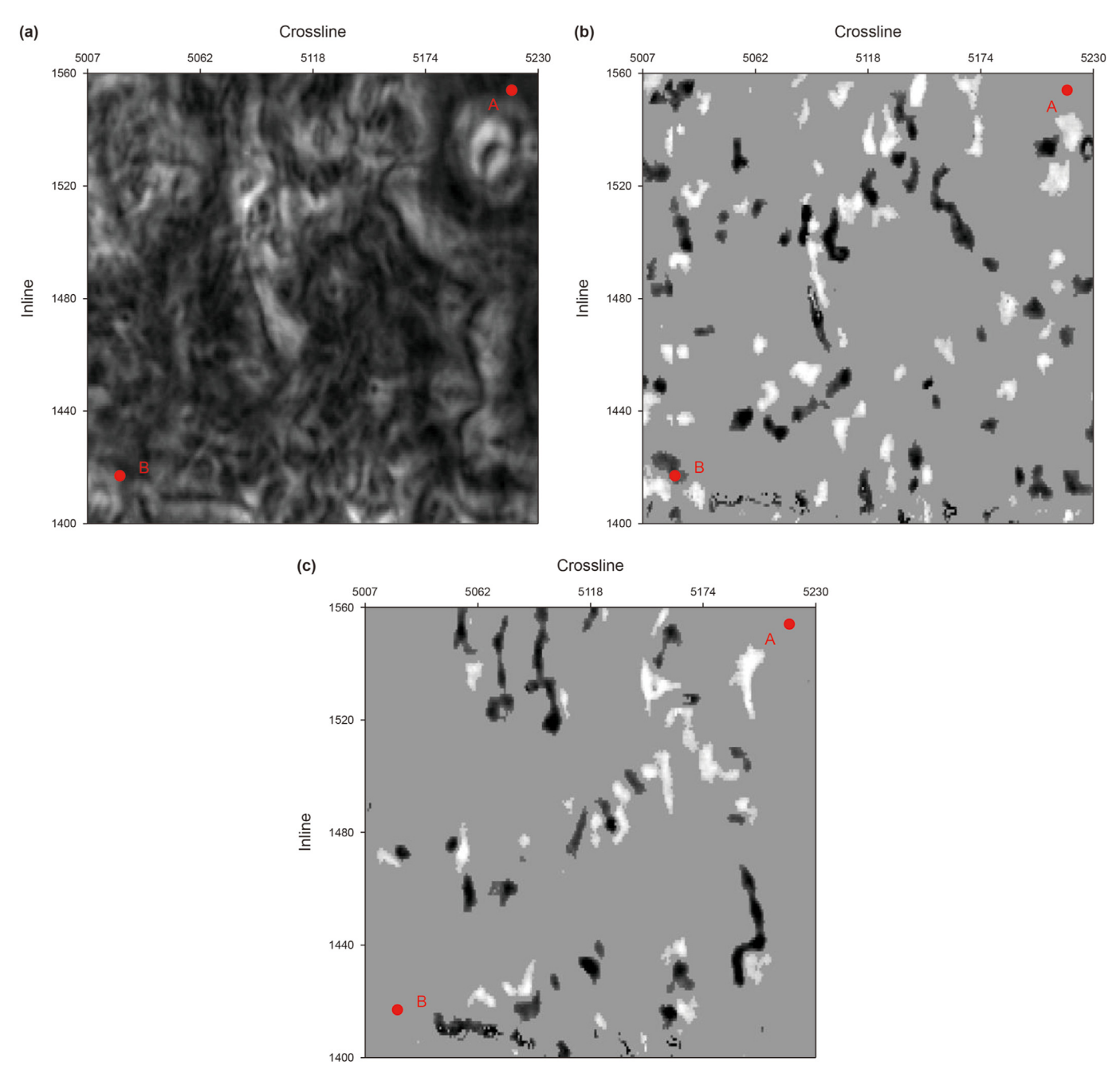


Fig. 24. (a) The seismic coherency attribute of field data. (b) The scatterer image using the proposed method. (c) The fault image using the proposed method.

equal to 5% in migration velocity, diffracted and scattered waves are almost completely unfocused. The DC-Net is difficult to correctly classify diffracted and scattered waves, as shown in Fig. 26(c), (d), (g), and (h). We use evaluation metrics such as accuracy, precision, recall, and F1-score to quantitatively evaluate the performance of the DC-Net when migration velocity is inaccurate. Table 2 presents the prediction performance of the DC-Net when migration velocity is inaccurate. When velocity errors are 2%, precision, recall, and F1-score exhibit minor degradation. With 5% velocity errors, these metrics demonstrate significant deterioration. This indicates that DC-Net struggles to accurately classify diffracted and scattered waves in the presence of substantial velocity errors. It is worth noting that all training dataset is generated using the correct migration velocity, which proves to some extent that the robustness of the proposed method when errors are small in migration

velocity.

We also conducted experiments on synthetic data contaminated by Gaussian random noise. We add different levels of random noise to the synthetic data and obtain the synthetic data with SNR of 10, 20, 25, and 30. We classify diffracted and scattered waves on these synthetic data with different SNR. The separated diffraction and diffraction image are shown in Fig. 27. Random noise masks deep diffracted and scattered waves to some extent, especially below 800 ms. The corresponding diffracted and scattered wave probability images are shown in Fig. 28. Table 3 presents the prediction performance of the DC-Net when synthetic data is contaminated by random noise. When the synthetic data has an SNR of 10, the DC-Net fails to function effectively. Due to the influence of random noise, the DC-Net cannot recognize all faults on the synthetic data with SNR of 20. For synthetic data with a signal-to-noise ratio of 25,

the DC-Net only identifies a small portion of deep faults. Noise also affects the classification of scattered waves, and the amplitude of scattered waves in deeper areas is weaker compared to shallow areas. In deeper areas, noise tends to mask the characteristics of scattered waves more strongly. In Fig. 28(d) and (f), it can be observed that as the depth increases, the classification result of scattered waves deteriorates, and the scatterer located at the deepest position is not displayed on the scattered wave probability image of the synthetic data with SNR of 20. Only a small fraction of the deepest scatterer is identified on the scattered wave probability image of the synthetic data with SNR of 25. With the increase of SNR, the classification effect of the network is gradually improved, and an acceptable classification result is obtained on the synthetic

data with SNR of 30. The above experiments demonstrate that the proposed diffracted and scattered waves classification imaging method has certain requirements for the SNR of input data, and an acceptable classification result can be achieved for data with SNR higher than 25. In order to obtain better classification effect, the input data should be denoised first.

It is worth noting that the DC-Net used in the above tests was trained using azimuth-dip angle image matrices generated from noise free diffraction data and correct migration velocity. When constructing a training dataset, considering noise and velocity errors may result in a better performing DC-Net model, but more data also requires the longer training time, and the introduction of noise may also increase the difficulty of training.

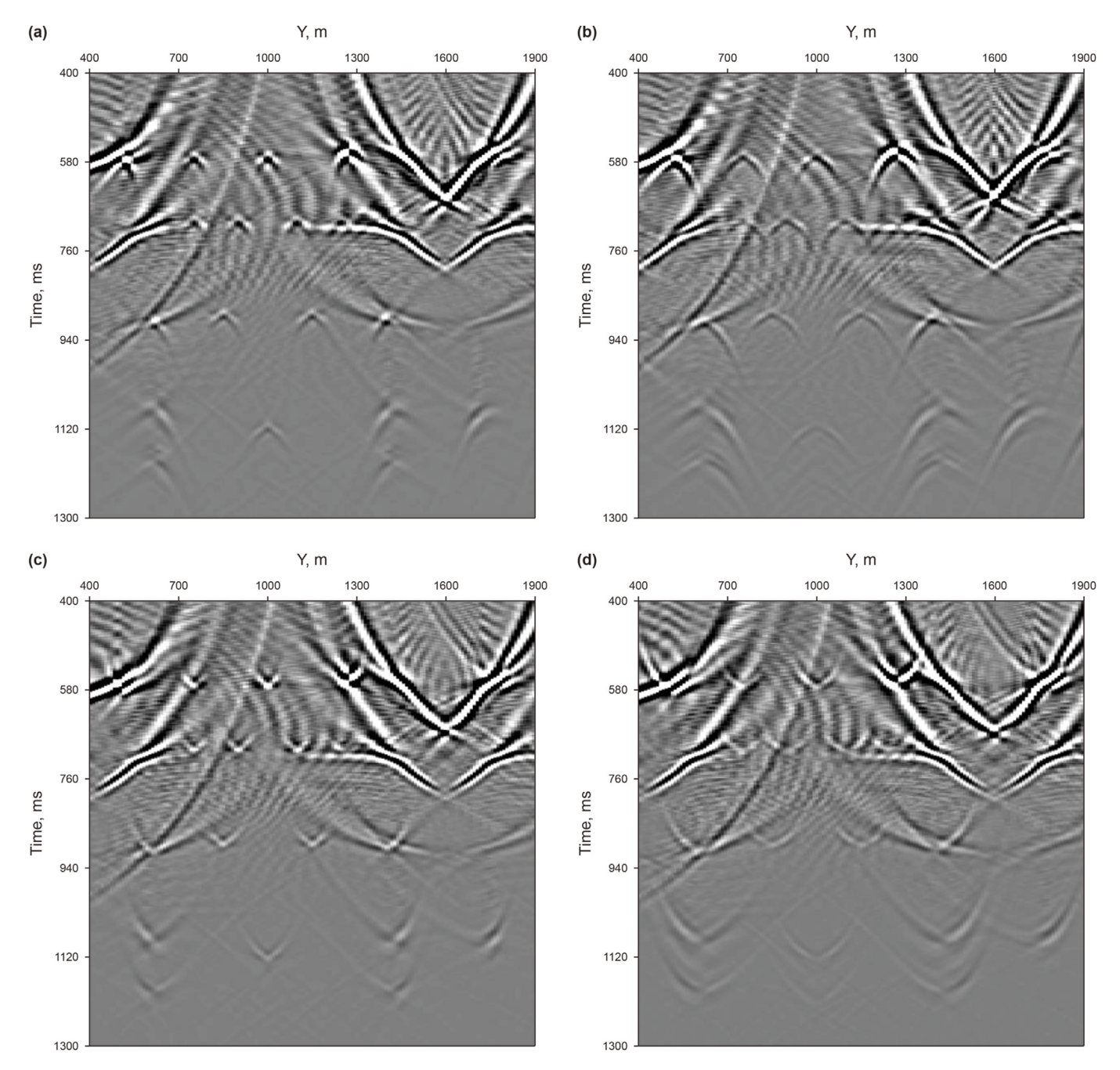


Fig. 25. The diffraction image profile at x = 500 m with inaccurate migration velocity: (a) 2% lower than the accurate migration velocity. (b) 5% lower than the accurate migration velocity. (c) 2% higher than the accurate migration velocity. (d) 5% higher than the accurate migration velocity.

T.-J. Sheng, J.-T. Zhao, S.-P. Peng et al. Petroleum Science 22 (2025) 2353–2383

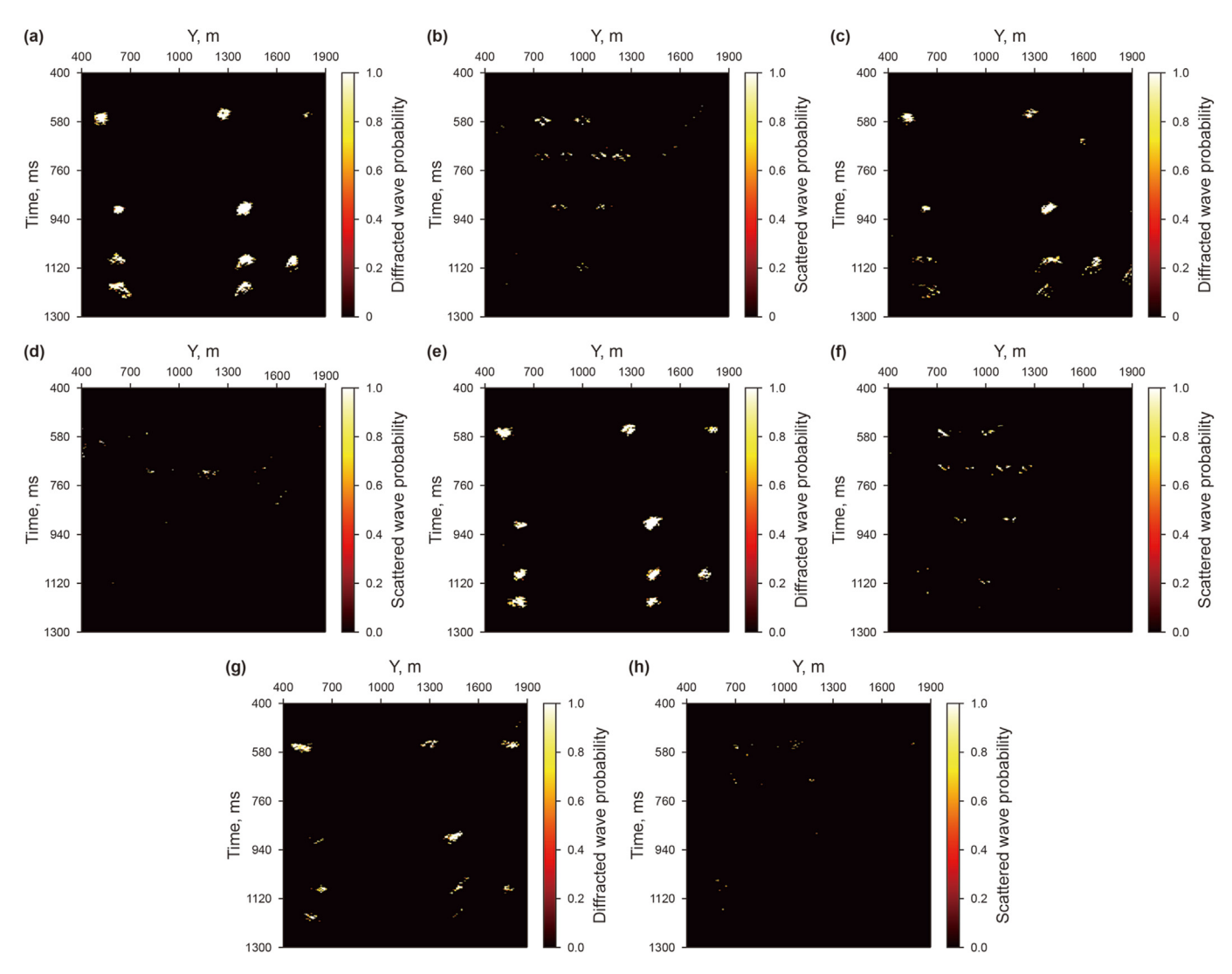


Fig. 26. The diffracted wave probability image profile at x = 500 m with inaccurate migration velocity; **(a)** 2% lower than the accurate migration velocity; **(c)** 5% lower than the accurate migration velocity; **(b)** 2% higher than the accurate migration velocity. The scattered wave probability image profile at x = 500 m with inaccurate migration velocity; **(b)** 2% lower than the accurate migration velocity; **(d)** 5% lower than the accurate migration velocity; **(f)** 2% higher than the accurate migration velocity; **(h)** 5% higher than the accurate migration velocity. The influence of errors in the migration velocity on the classification of scattered waves is greater than that of diffracted waves. The scattered waves can hardly be located on the scattered wave probability image when the errors are equal to 5%.

The DC-Net uses the azimuth-dip angle image matrix generated by the separated diffraction using the PWD method as the input, so the residual reflections contained in the separated diffraction may also affect the classification result. We adjusted the parameters of the PWD method to make more reflections remain in the separated diffractions. The imaging results of these separated diffractions containing residual reflections of different intensities are shown in Fig. 29. The red box indicates area with more residual reflections, which is stronger in Fig. 29(b) than in Fig. 29(a), and to some extent mask nearby scatterers. The scattered and diffracted wave probability images are shown in Fig. 30. Residual reflections have an

adverse effect on the classification results, and the stronger the residual reflections, the greater the impact in the classification results (area indicated by white boxes in Fig. 30(b) and (d)). However, even in the presence of strong residual reflections, the DC-Net can still correctly classify a small part of the scatterer, which shows that the proposed method has a certain robustness to residual reflections.

Further, we design an experiment to quantitatively analyze how varying residual reflection intensities affect the classification accuracy of the DC-Net. In order to quantitatively control the intensity of the reflected waves, we perform this experiment using a simple

Table 2Evaluation statistics of classification results of the DC-Net when migration velocity is inaccurate.

Evaluation, %	Accurate velocity	2% lower velocity	2% higher velocity	5% lower velocity	5% higher velocity
Accuracy	96.03	95.78	95.37	94.94	94.54
Precision	88.16	86.65	83.12	60.32	55.21
Recall	54.76	51.08	47.70	40.58	36.94
F1-score	62.71	57.70	53.49	43.87	38.58

T.-J. Sheng, J.-T. Zhao, S.-P. Peng et al. Petroleum Science 22 (2025) 2353–2383

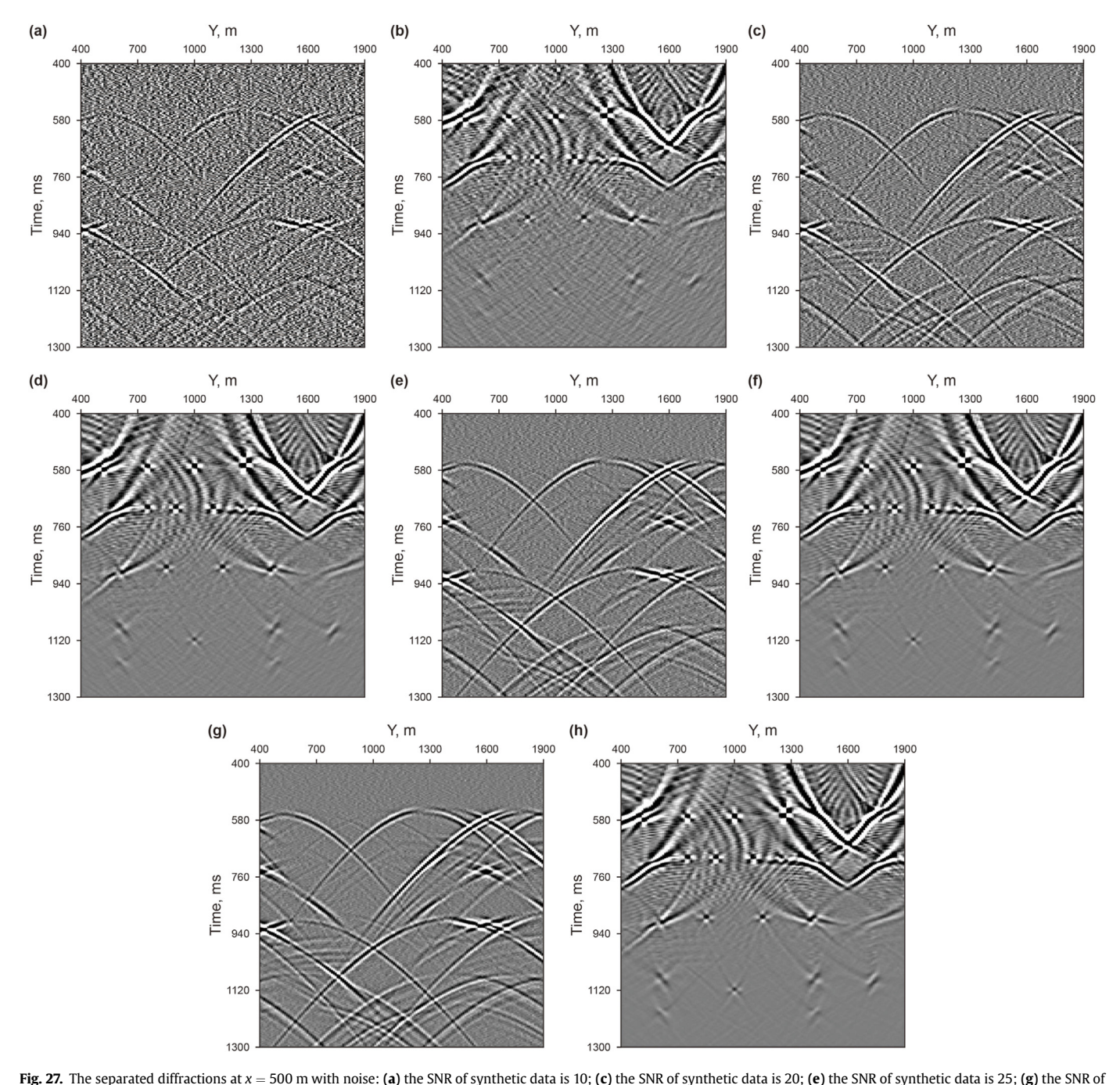


Fig. 27. The separated diffractions at x = 500 m with noise: (a) the SNR of synthetic data is 10; (c) the SNR of synthetic data is 20; (e) the SNR of synthetic data is 20; (f) the SNR of synthetic data is 20; (f) the SNR of synthetic data is 20; (f) the SNR of synthetic data is 20; (h) the SNR of synthetic data is 30.

model containing 4 scatterers, 5 faults, and a horizontal reflector (as shown in Fig. 31). The model contains only the horizontal reflector, we can easily obtain the accurate dip angle (since the dip angle of the horizontal reflector is 0). We use the PWD method to extract diffractions based on the accurate dip angle. Since the dip angle is accurate, we treat diffraction extracted by the PWD method as pure diffraction data that does not contain reflections. The reflection data is obtained by subtracting the pure diffraction data using the full wavefield data. To test the effect of residual reflections, we apply different amplitude weights to the reflection data to construct the reflection data with different intensities, with amplitude weights of 0%, 20%, 40%, 60%, 80%, and 100%,

respectively. These 6 weighted reflection data are summed with the pure diffraction data to obtain the test data containing 0%, 20%, 40%, 60%, 80%, and 100% intensity residual reflections. The construction process of test data can be described by the following equation:

$$test = diffr + \gamma \times refl, \tag{23}$$

where **test** is test data. The **diffr** is pure diffraction data and **refl** is reflection data. The γ is amplitude weight (0%, 20%, 40%, 60%, 80%, and 100%).

We test the DC-Net on these 6 test data containing residual reflections with different intensities. Table 4 presents the

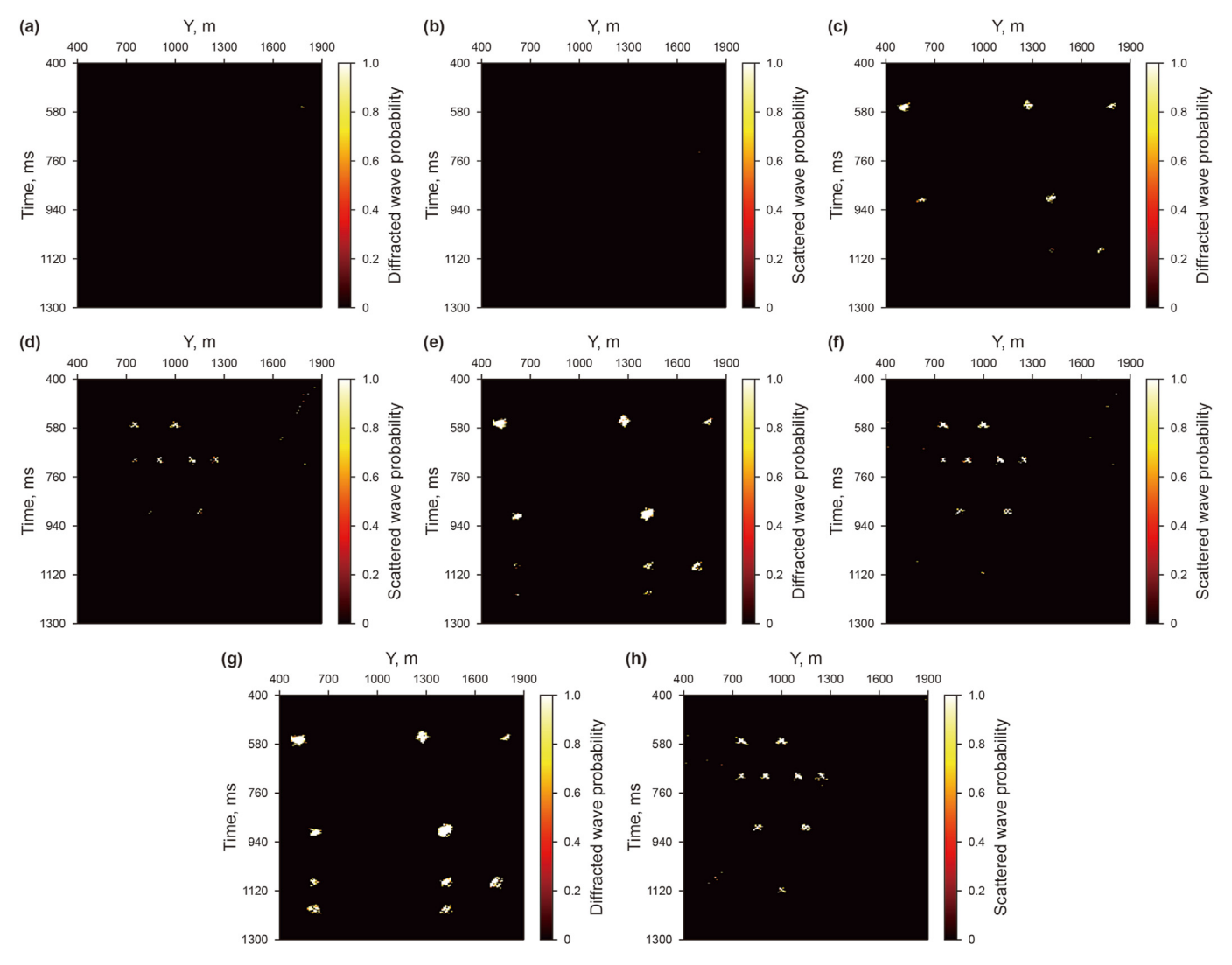


Fig. 28. The diffracted wave probability image profiles: (a) the SNR of synthetic data is 10; (c) the SNR of synthetic data is 20; (e) the SNR of synthetic data is 25; (g) the SNR of synthetic data is 30. The scattered wave probability image profiles: (b) the SNR of synthetic data is 10; (d) the SNR of synthetic data is 20; (f) the SNR of synthetic data is 20; (f) the SNR of synthetic data is 30.

Table 3Evaluation statistics of classification results of the DC-Net when test data is contaminated by random noise.

Evaluation, %	SNR = 10	SNR = 20	SNR = 25	SNR = 30
Accuracy	94.64	95.07	95.49	95.82
Precision	48.21	91.19	91.99	91.14
Recall	33.35	39.33	45.13	50.31
F1-score	32.45	43.40	52.16	58.53

prediction performance of the DC-Net on these 6 test data. The classification results of 4 test data are shown in Fig. 32. As the intensity of the residual reflections increases, the probability that the residual reflections are determined to be diffracted waves or scattered waves also increases. Until the intensity of the residual reflections increases to 60%, diffracted wave and scattered wave probability images can still outline faults and scatterers relatively effectively. It demonstrates the robustness of the DC-Net to residual reflections. When dealing with real data, pure diffraction data are difficult to obtain. The robustness to residual reflections favors the extension of the proposed method to practical applications.

In previous experiments, the azimuth-dip angle image matrices used for DC-Net training and processing were 2-dimensional 181×181 matrices. Here, we first test the effect of test data resolution on the classification results of DC-Net. For the convenience of the subsequent description, we name the training dataset used in the numerical examples (training data are 2-dimensional 181×181 matrices) as D0 and the test dataset used in the numerical examples as T0. The DC-Net trained using the training dataset D0 is named as DC-Net0. We perform dip and azimuth angle direction's equidistant downsampling with a spacing of 2, 4 and 8 on the test dataset T0to generate test dataset T2, T4, and T8, which are shown in Fig. 33. We use DC-Net0 to process the test dataset T2, T4, and T8, respectively. The prediction results are shown in Fig. 34. Due to the fact that the sampling interval of all azimuth-dip angle image matrices in the training dataset D0 is 1°, the performance of DC-Net0 on the test dataset T2, T4, T8 is quite poor. There is no valid information in the predicted diffracted and scattered probability images. This indicates that DC-Net0 is highly sensitive to the resolution of the input azimuth-dip angle image matrix. Adding the azimuth-dip angle image matrix with other sampling intervals to the training dataset may help improve the robustness of DC-Net to

T.-J. Sheng, J.-T. Zhao, S.-P. Peng et al. Petroleum Science 22 (2025) 2353—2383

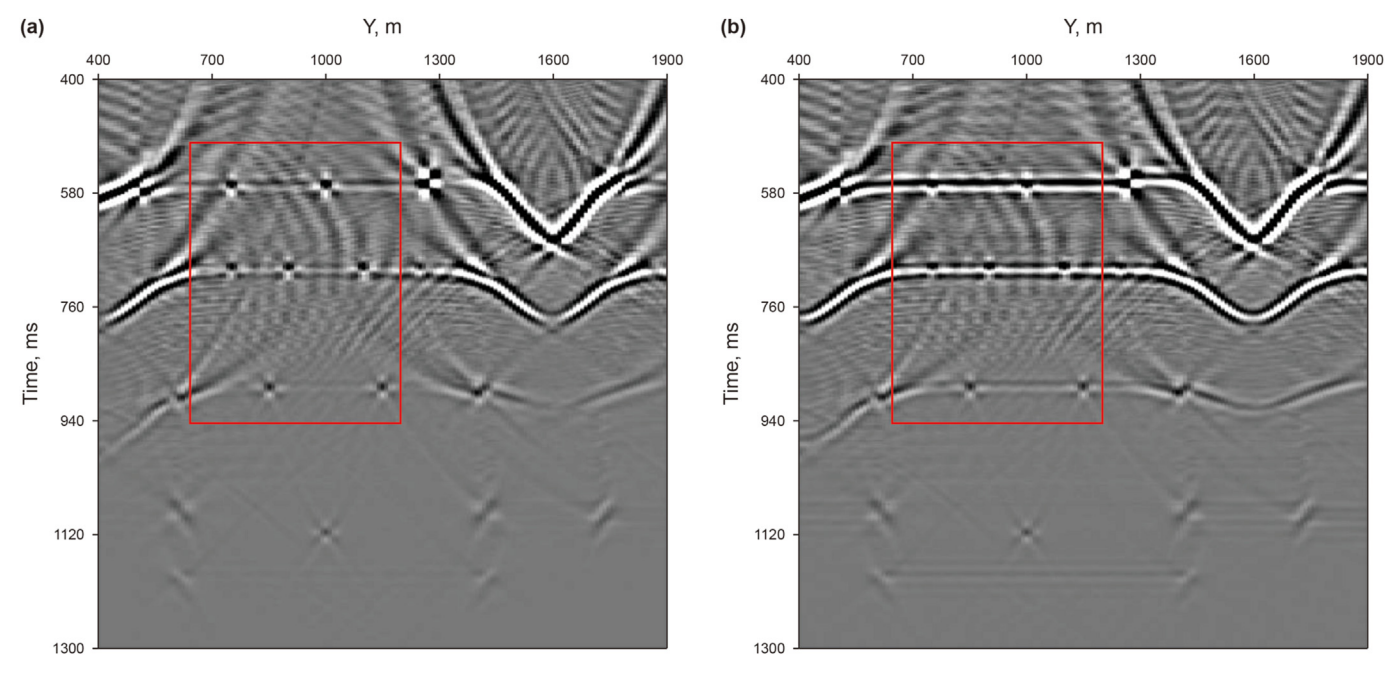


Fig. 29. (a) The diffraction image contains weak residual reflections (at x = 500 m); **(b)** The diffraction image contains strong residual reflections (at x = 500 m). The red box indicates the area with residual reflections.

resolution of the input azimuth-dip angle image matrix. The number of sampling points of the azimuth-dip angle image matrix has a significant impact on the time spent on training DC-Net. Fewer sampling points means fewer operations, but the resolution of the azimuth-dip angle image matrix in the training dataset is also lower, which is likely to affect the performance of the DC-Net. This seems to lead to a trade-off between training efficiency and network performance. Therefore, we discuss the effect of the number of sampling points of the azimuth-dip angle image matrix in the training dataset on the performance of the DC-Net. We perform dip and azimuth angle direction's equidistant downsampling with a spacing of 2, 4 and 8 on the training dataset D0to construct the training datasets D2, D4, and D8. Then, we train the DC-Net using D2, D4, and D8 to obtain DC-Net2, DC-Net4, and DC-Net8, respectively. It can be seen that the resolution of the azimuthdip angle image matrix gradually decreases with the increase of the downsampling spacing, and kinematic and dynamic characteristics of scattered and diffracted waves become less and less obvious. We use DC-Net2, DC-Net4, and DC-Net8 to process the test dataset T2, T4, and T8, respectively. The prediction results are shown in Fig. 35. The diffracted wave probability image predicted by the DC-Net2 clearly reveal the positions of faults, while the scattered wave probability image predicted by the DC-Net2 cannot reveal all scatterers. As the downsampling interval gradually increases, the prediction results deteriorate. The results predicted by the DC-Net4 can only reveal a few faults, but cannot reveal the location of scatterers. The prediction results of the DC-Net8 are the worst, and effective information about faults and scatterers cannot be obtained from the diffracted and scattered wave probability images predicted by the DC-Net8. It indicates that when the resolution of the azimuth-dip angle image matrix in the training dataset is too low, the DC-Net cannot learn the effective characteristics of scattered and diffracted waves from the training dataset. Considering the training efficiency and network performance, we believe that the sampling interval between the dip and azimuth angle directions of the azimuth-dip angle image matrix in the training dataset should be less than 2°.

Learning rate and batch size are key hyperparameters, and

certain network structures may be sensitive to learning rate and batch size, to the extent that they not only affect the training process of the network but also its performance on test data. Here, we conduct two sets of experiments to analyze the effect of learning rate and batch size on the DC-Net. In the first set of experiments, we test the effect of learning rate on the DC-Net. We set the initial learning rates to 0.1, 0.01, and 0.001 to train the DC-Net and use the trained DC-Net to process the test data. In this set of experiments, other hyper-parameters, training dataset remain unchanged (same as the numerical examples section). The training and validation loss curves with different learning rates are shown in Fig. 36. Larger learning rates cause the DC-Net to converge at a lower rate during training, and the model at an initial learning rate of 0.1 significantly requires more epochs to bring the training loss down to the level of learning rates of 0.01 and 0.001. In addition, Fig. 36(b) demonstrates that a large learning rate causes a larger oscillation in the validation loss of the DC-Net. Table 5 presents the prediction performance of these DC-Nets on test data. The recall rate and F1 score are relatively greatly affected by changes in the learning rate. This implies that the prediction performance of the DC-Net is sensitive to the learning rate. The second set of experiments we test the effect of the batch size on the DC-Net, we set the batch sizes to 8.16. 32 to train DC-Net and use the trained DC-Net to process the test data. Similarly, in this set of experiments, other hyperparameters, and training dataset remain the same (as in the numerical examples section). The training and validation loss curves with different batch sizes are shown in Fig. 37. In Fig. 37(a), the three training loss curves almost overlap. While the validation loss curve shown in Fig. 37(b) reveals that smaller batch size may cause instability in validation loss. Table 6 presents the prediction performance of these DC-Nets on test data. These 4 scores are similar for training the DC-Net using initial learning rates 0.1, 0.01, and 0.001. This implies that the prediction performance of the DC-Net is less sensitive to the batch size. This parameter analysis experiment suggests that the learning rate and batch size should be set carefully when training the DC-Net, and that finding a suitable set of hyperparameter combinations (e.g., grid-search methods) can help to train a DC-Net with stronger generalization capabilities.

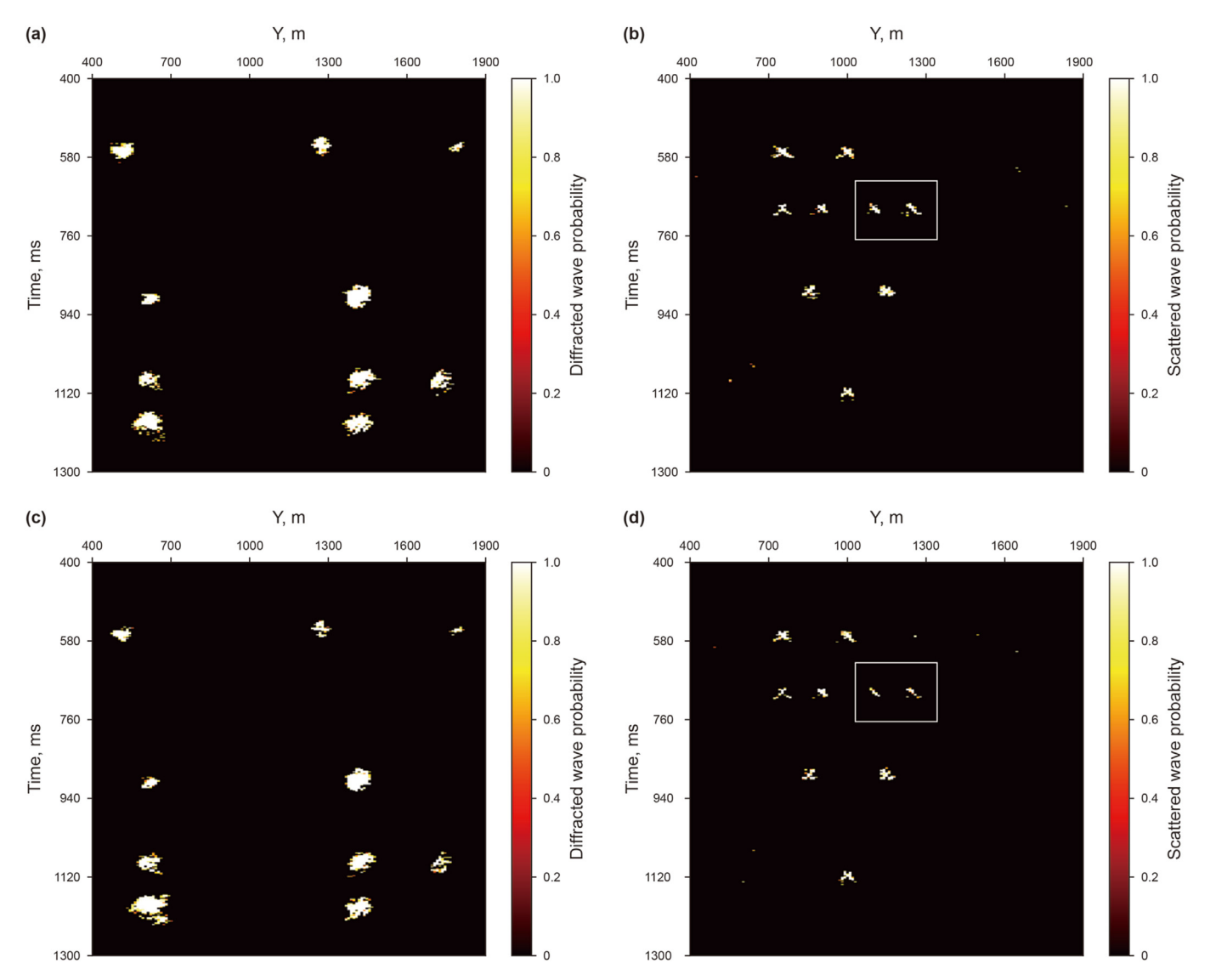


Fig. 30. (a) The diffracted wave probability image of data containing weak residual reflections (at x = 500 m); (b) The scattered wave probability image of data containing weak residual reflections (at x = 500 m); (c) The diffracted wave probability image of data containing strong residual reflections (at x = 500 m); (d) The scattered wave probability image of data containing strong residual reflections (at x = 500 m); (d) The scattered wave probability image of data containing strong residual reflections (at x = 500 m).

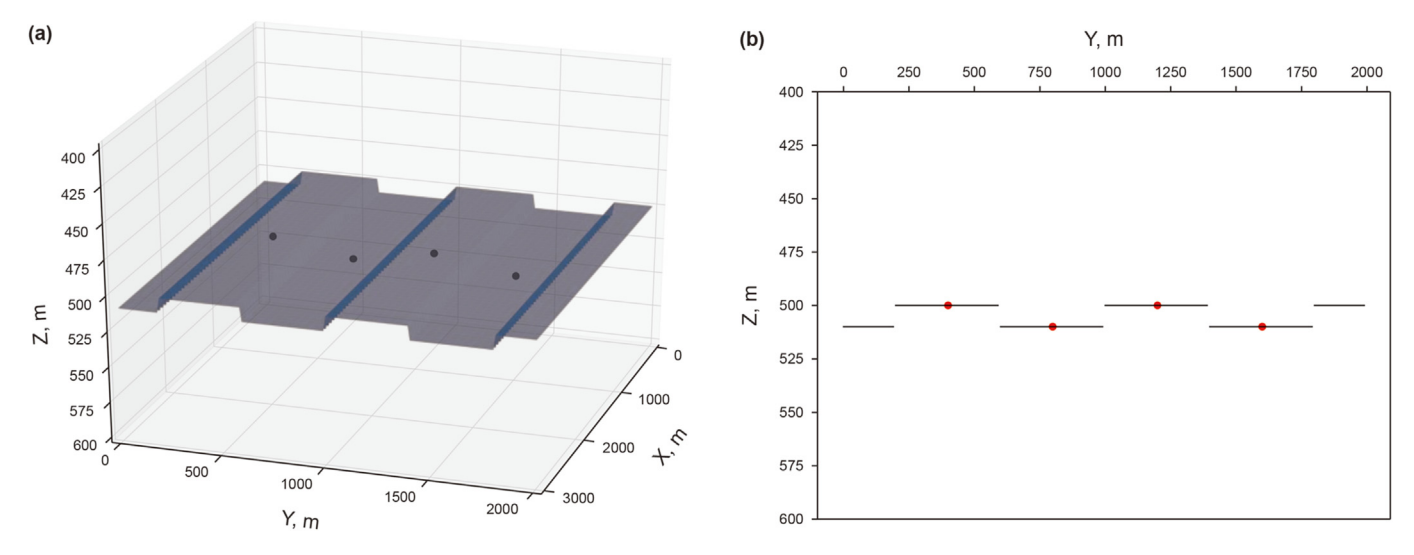


Fig. 31. The simple model with 4 scatterers, 5 faults, and a horizontal reflector. (a) The 3D simple geological model. (b) The YZ reflectivity section at x = 1500 m. Black lines represent reflectors whose reflectivity is 1.0. Red dots represent scatterers with a radius of 5 m, and their reflectivity is set to 2. The size of faults is set to 10 m.

Table 4Evaluation statistics of classification results of the DC-Net on the test data containing different intensity residual reflections.

Evaluation, %	0% intensity	20% intensity	40% intensity	60% intensity	80% intensity	100% intensity
Accuracy	90.76	87.27	83.54	79.83	77.83	76.40
Precision	86.79	77.19	70.50	63.27	59.04	56.08
Recall	79.87	76.02	67.90	61.48	57.75	54.97
F1-score	82.80	76.57	69.06	62.31	58.37	55.47

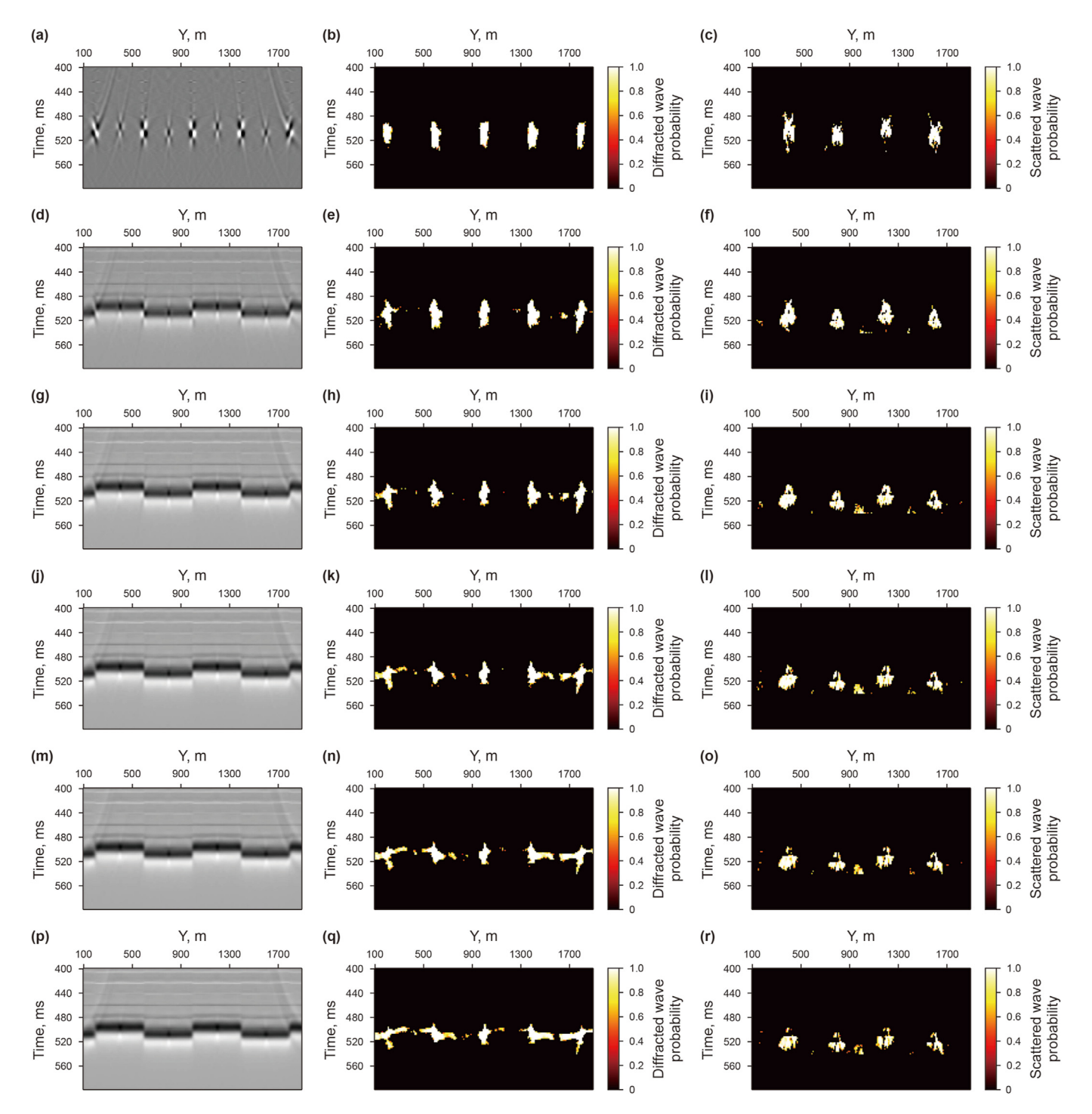


Fig. 32. The classification results of 6 test data at x = 1500 m. The **(a), (d), (g), (j), (m)**, and **(p)** are diffraction images with 0%, 20%, 40%, 60%, 80%, and 100% intensity of residual reflections, respectively. The **(b), (e), (h), (k), (n)**, and **(q)** are diffracted wave probability images of test data with 0%, 20%, 40%, 60%, 80%, and 100% intensity of residual reflections, respectively. The **(c), (f), (i), (l), (o)**, and **(r)** are scattered wave probability images of test data with 0%, 20%, 40%, 60%, 80%, and 100% intensity of residual reflections, respectively.

T.-J. Sheng, J.-T. Zhao, S.-P. Peng et al. Petroleum Science 22 (2025) 2353–2383

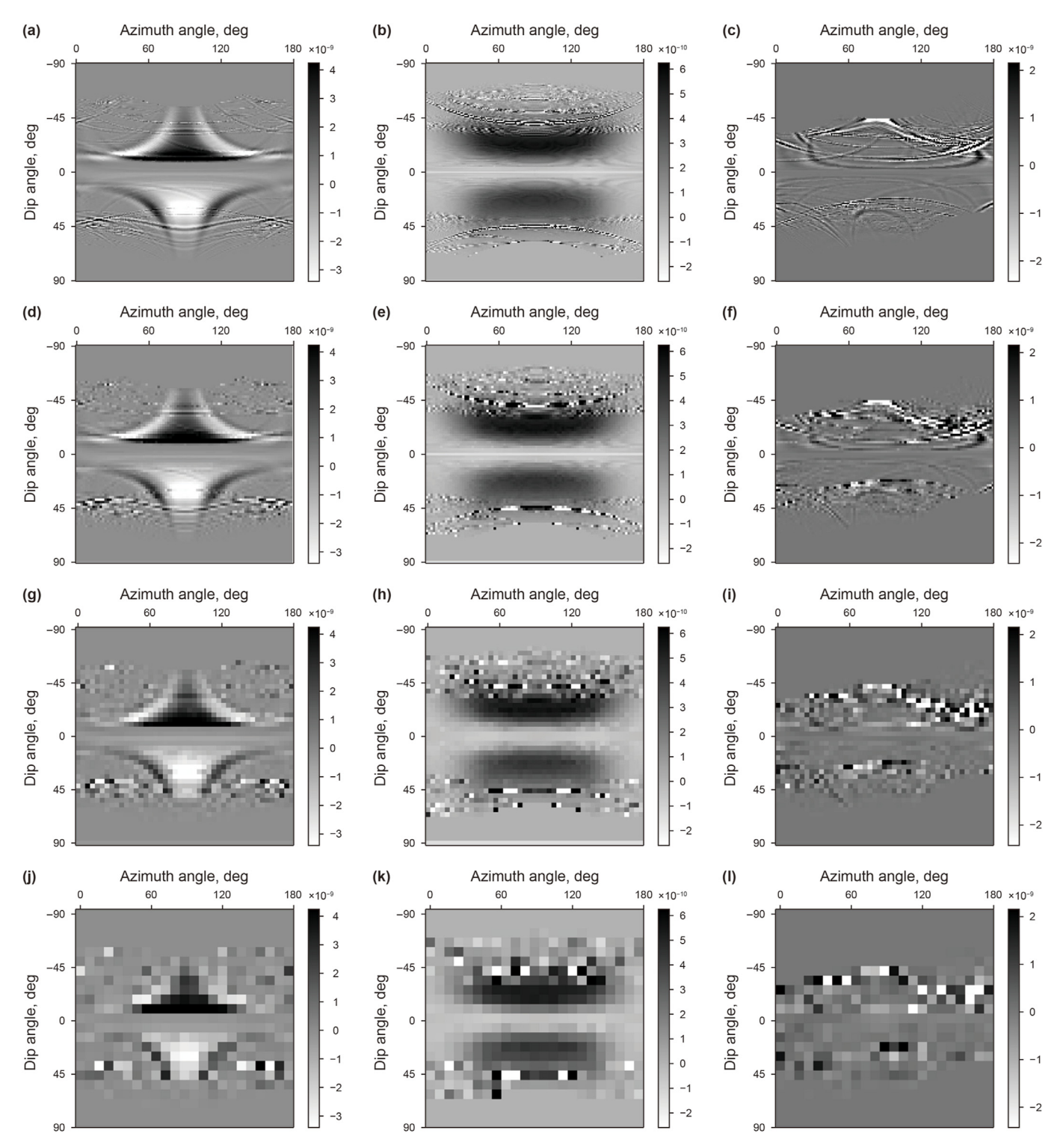


Fig. 33. The azimuth-dip angle image matrices of T0, T2, T4, and T8. The (a), (d), (g), and (j) are the diffracted wave of T0, T2, T4, and T8, respectively. The (b), (e), (h), and (k) are the scattered wave of T0, T2, T4, and T8, respectively. The (c), (f), (i), and (l) are the residual reflection of T0, T2, T4, and T8, respectively.

Traditional seismic attribute and diffraction imaging techniques are designed to enhance discontinuities in seismic images and do not distinguish whether these discontinuities are scattered or diffracted waves. The identification of faults and scatterers based on seismic attribute techniques and diffraction imaging techniques often relies on manual interpretation. The proposed method realizes automatic classification and identification of faults and

scatterers based in diffraction images using deep learning techniques. It improves the resolution of faults and scatterers compared to traditional methods, as well as reduces the dependence on manual interpretation. Although DC-Net classifies scattered and diffracted waves on the basis of diffraction images, it is robust to residual reflected waves. When dealing with real data, pure diffraction images are difficult to obtain and residual reflections are

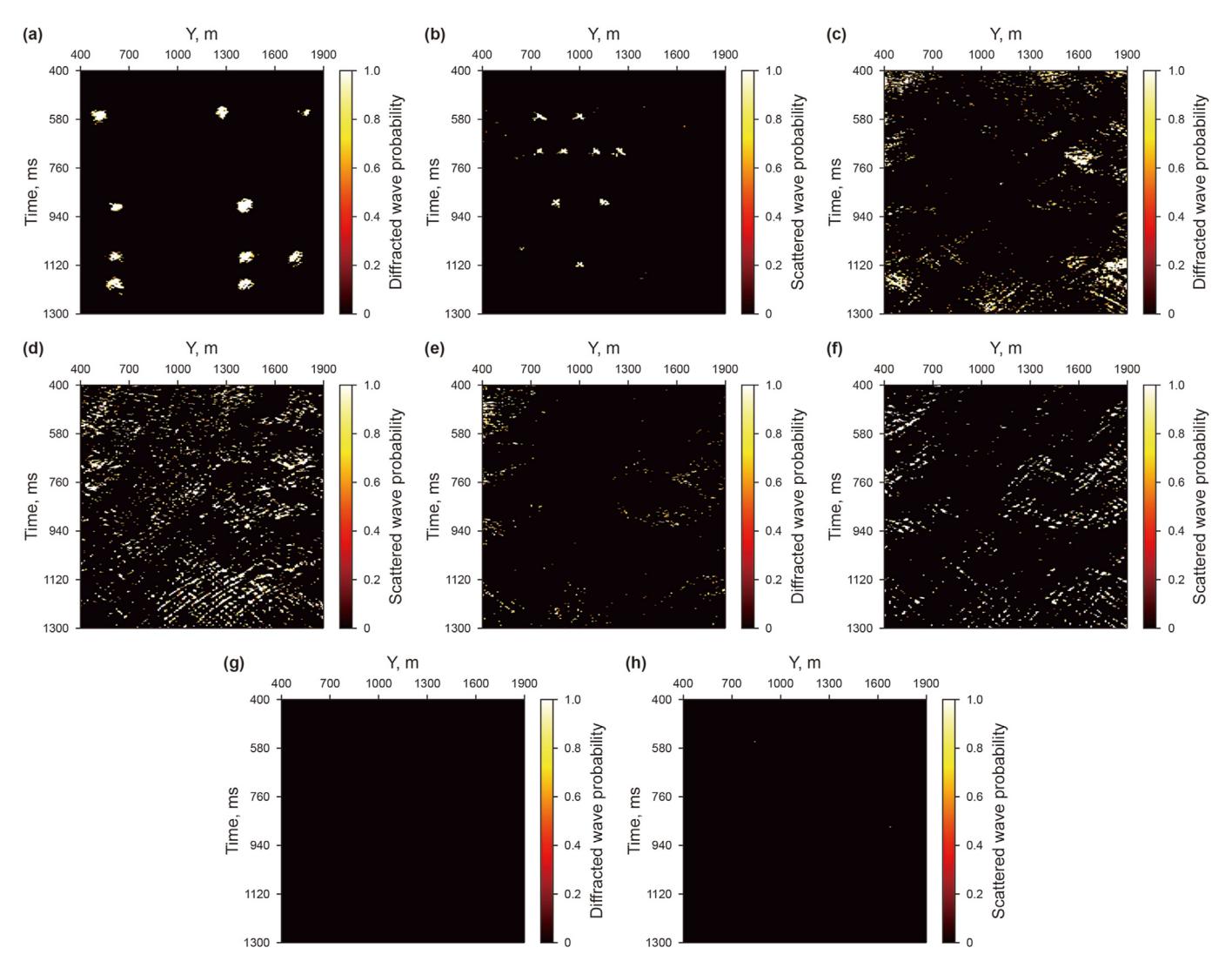


Fig. 34. The prediction results of DC-Net0 on test dataset T0, T2, T4, and T8. The (a) and (b) are the diffracted and scattered wave probability images of test dataset T0, respectively. The (c) and (d) are the diffracted and scattered wave probability images of test dataset T2, respectively. The (e) and (f) are the diffracted and scattered wave probability images of test dataset T4, respectively. The (g) and (h) are the diffracted and scattered wave probability images of test dataset T8, respectively.

often present in diffraction images. This robustness is beneficial for practical applications of the DC-Net.

However, the DC-Net still has some shortcomings. As a deep learning model, the performance of the DC-Net depends on the training dataset. If noise, velocity errors, and resolution of azimuth-dip angle image matrices are not considered when constructing a training dataset, the trained DC-Net will be sensitive to these three factors. The impact of resolution is the largest among these three factors. The DC-Net trained only with high-resolution azimuth-dip angle image matrices cannot effectively distinguish between scattered waves and diffracted waves in low resolution azimuth-dip angle image matrices. This will result in classification failure. Considering these three factors when building the training dataset means increasing the number of samples. It results that more effort will be required in training network.

The classification of faults and scatterers is achieved based on each imaging point. DC-Net classifies azimuth-dip angle image matrices of one imaging point at a time. The forward modeling may cause a dispersion effect in synthetic data. This dispersion effect can lead to corresponding noise in azimuth-dip angle image matrices. However, the field data is virtually devoid of this noise

introduced by the forward modeling algorithm. It means that there is an inherent error between synthetic training dataset and field data. Despite inherent errors, the knowledge related to characteristics of diffracted and scattered waves learned from the synthetic data can still be transferred to field data. The introduction of transfer learning has to some extent alleviated the problems caused by this forward modeling algorithm. Of course, the smaller the inherent error, the better the network's performance on field data should be. Therefore, using high-precision forward modeling methods to construct training datasets is beneficial for improving the performance of network on field data. Our future efforts are to eliminate this noise through higher precision forward algorithms, denoising algorithms, or new migration methods.

In fact, diffractors (faults, fractures, etc.) have better geometric extension compared to scatterers. This is another valid feature for distinguishing scatterers and diffractors (including fault planes) along layers or time slices. In order to utilize this valid feature, time-space coherence between the imaging points should be considered. From a geometrically constrained point of view, considering the time-space coherence between imaging points should result in a better characterization of fault planes. However,

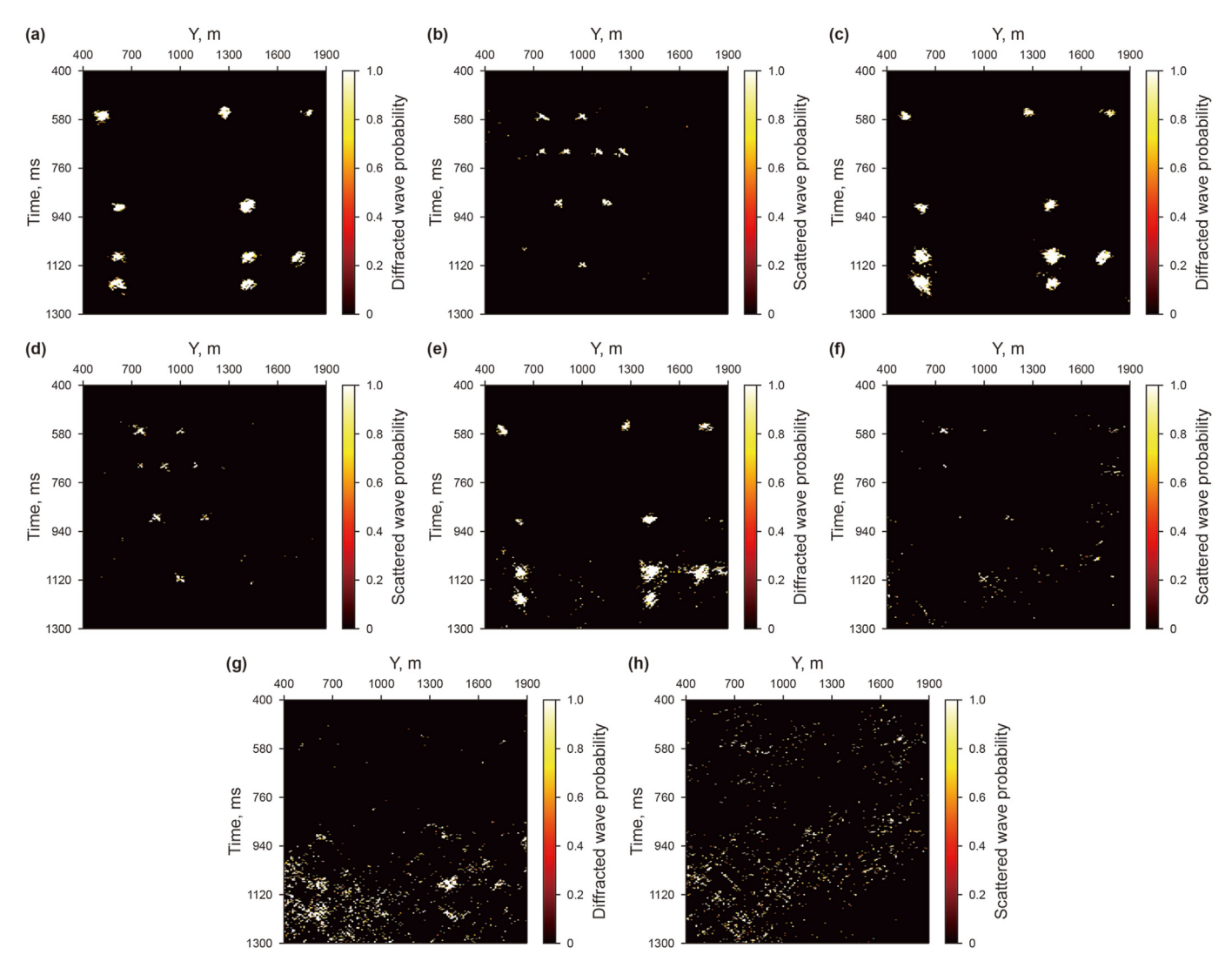


Fig. 35. The prediction results of DC-Net0, DC-Net2, DC-Net4, DC-Net8. The (a) and (b) are the diffracted and scattered wave probability images predicted by the DC-Net0, respectively. The (c) and (d) are the diffracted and scattered wave probability images predicted by the DC-Net2, respectively. The (e) and (f) are the diffracted and scattered wave probability images predicted by the DC-Net4, respectively. The (g) and (h) are the diffracted and scattered wave probability images predicted by the DC-Net8, respectively.

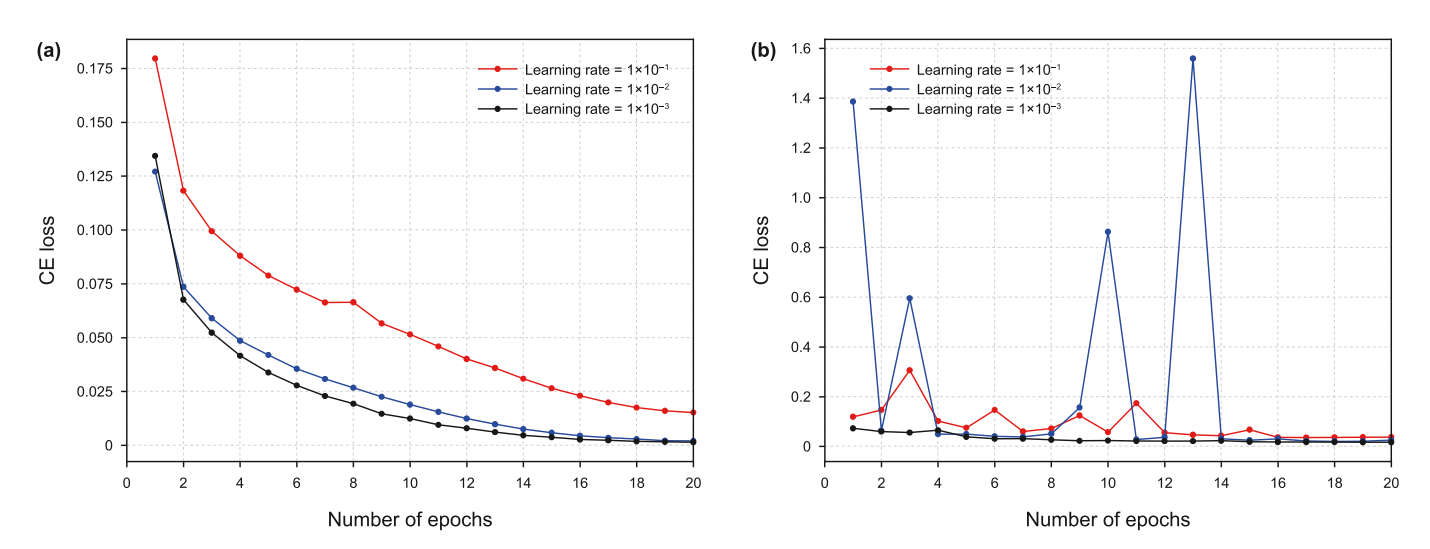


Fig. 36. The training and validation loss curves in learning rate analysis experiment.

Table 5Evaluation statistics of classification results of the DC-Net trained with different learning rate on test data.

Evaluation, %	Learning rate is 0.1	Learning rate is 0.01	Learning rate is 0.001
Accuracy	95.69	95.53	96.03
Precision	84.07	87.78	88.16
Recall	52.95	49.12	54.76
F1-score	60.43	55.53	62.71

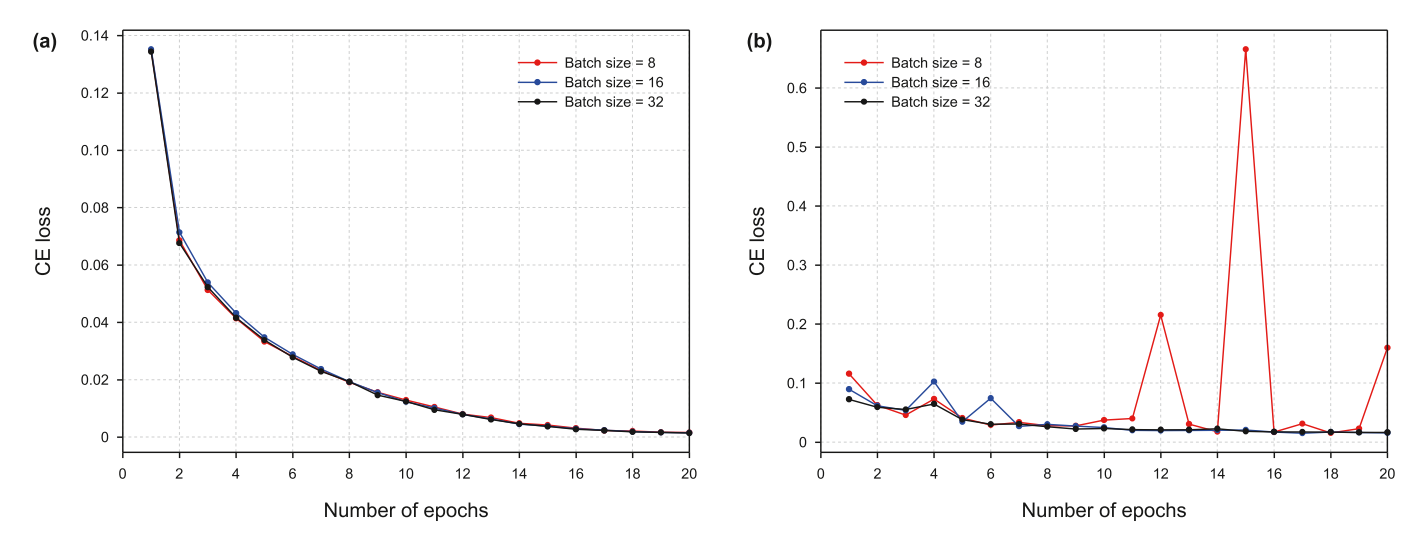


Fig. 37. The training and validation loss curves in batch size analysis experiment.

Table 6Evaluation statistics of classification results of DC-Net trained with different batch size on test data.

Evaluation, %	Batch size is 8	Batch size is 16	Batch size is 32
Accuracy	95.77	95.68	96.03
Precision	84.21	86.21	88.16
Recall	56.58	54.94	54.76
F1-score	63.39	61.15	62.71

considering time-space coherence is unfavorable for training the DC-Net and using the DC-Net for prediction. If time-space coherence between imaging points is considered, the input data of the DC-Net will be a function of position (x, y, τ) , dip angle θ and azimuth angle φ . The input data is a 5D matrix. This puts a huge computational burden on the training network, and therefore training can be very time-consuming. In addition, for the 5D matrix, the whole training data must be split with small window in both temporal and spatial directions. A small part of training data in small window is used for training. The criteria for splitting training data are also difficult to determine. This computational pressure is also reflected in network prediction. When using DC-Net for prediction, it is not possible to predict the whole test data directly on a GPU device because the test data is a 5D matrix. Therefore, it is inevitable to split the test data, splitting the whole test data into multiple small data cubes and predicting one small data cube at a time. Different split methods may also affect the classification results of the DC-Net and increase the instability of the classification results. Neglecting time-space coherence has an impact on the classification and identification of fault planes, which is a limitation of our method. Our future efforts are to find a way to address this limitation and enhance the recognition of fault planes by considering time-space coherence between imaging points.

5. Conclusion

In this paper, in order to accurately locate tiny faults or scatterers, a diffraction classification imaging method using a DC-Net in the azimuth-dip angle image matrix is proposed. The azimuth-dip angle image matrix preserves the dynamic and azimuth characteristics of the wavefield, making it easier to classify diffracted and scattered waves. We construct a DC-Net to classify diffracted and scattered waves in the azimuth-dip angle image matrix. The DC-Net uses dense connections to improve flow of feature information and apply coordinate attention to obtain direction aware and position sensitive information about diffracted and scattered waves. Thus, DC-Net can effectively utilize azimuth angle and polarity differences to classify diffracted and scattered waves. The proposed method achieves high-accuracy automatic classification of cavities and faults based on diffraction imaging. The numerical experiment of 3D geologic model validates the fine performance of the proposed diffraction classification imaging method in the diffraction image in the presence of complex geologic structures. The field data application demonstrates DC-Net is ability to accurately classify scatterers and faults in the diffraction image, further enhances the resolution of diffraction image, and is beneficial for the development of karst fracture-cavern reservoirs.

CRediT authorship contribution statement

Tong-Jie Sheng: Writing — review & editing, Writing — original draft, Methodology. **Jing-Tao Zhao:** Supervision, Funding acquisition, Conceptualization. **Su-Ping Peng:** Supervision. **Zong-Nan Chen:** Data curation. **Jie Yang:** Software.

Declaration of competing interest

The authors declare that they have no known competing

financial interests or personal relationships that could have appeared to influence the work reported in this paper.

Acknowledgments

This work is supported by Science Fund for Creative Research Groups of the National Natural Science Foundation of China, No. 42321002.

References

- Bashir, Y., Waheed, U.B., Ali, S.H., et al., 2024. Enhanced wave modeling & optimal plane-wave destruction (OPWD) method for diffraction separation and imaging. Comput. Geosci. 187, 1–11. https://doi.org/10.1016/j.cageo.2024.105576.
- Bleistein, N., Cohen, J., Stockwell, W., 2001. Mathematics of Multidimensional Seismic Imaging, Migration, and Inversion. Springer, Berlin, Germany.
- Chen, X., Cao, J.J., Yang, H.L., et al., 2022a. Diffraction separation and imaging based on double sparse transforms. Pet. Sci. 19 (2), 534–542. https://doi.org/10.1016/j.petsci.2021.12.002.
- Chen, W., Liu, X., Saad, O.M., et al., 2022b. 3-D seismic diffraction separation and imaging using the local rank-reduction method. IEEE Trans. Geosci. Rem. Sens. 60, 1–10. https://doi.org/10.1109/TGRS.2021.3139314.
- Chen, Z.N., Zhao, J.T., Peng, S.P., et al., 2024. Diffraction imaging method using curvelet-domain cascade filter. Pure Appl. Geophys. 181, 1241–1257. https://doi.org/10.1007/s00024-024-03456-6.
- Chen, Z.N., Zhao, J.T., Peng, S.P., et al., 2023. Separating seismic diffractions by an improved Cook-distance singular value decomposition method. Geophysics 88 (1), WA377—WA386. https://doi.org/10.1190/geo2022-0284.1.
- Cheng, J.B., Wang, T.F., Wang, C.L., et al., 2012. Azimuth-preserved local angle-domain prestack time migration in isotropic, vertical transversely isotropic and azimuthally anisotropic media. Geophysics 77 (2), S51—S64. https://doi.org/10.1190/geo2011-0295.1.
- Cheng, J.B., Geng, J.H., Wang, H.Z., et al., 2011. 3D Kirchhoff prestack time migration in average illumination-azimuth and incident-angle domain for isotropic and vertical transversely isotropic media. Geophysics 76 (1), S15–S27. https:// doi.org/10.1190/1.3533913.
- Cunha, A., Pochet, A., Lopes, H., et al., 2020. Seismic fault detection in real data using transfer learning from a convolutional neural network pre-trained with synthetic seismic data. Comput. Geosci. 135, 1–9. https://doi.org/10.1016/ j.cageo.2019.104344.
- de Figueiredo, J.J.S., Oliveira, F., Esmi, E., et al., 2013. Automatic detection and imaging of diffraction points using pattern recognition. Geophys. Prospect. 61, 368–379. https://doi.org/10.1111/j.1365-2478.2012.01123.x.
- Decker, L., Janson, X., Fomel, S., 2015. Carbonate reservoir characterization using seismic diffraction imaging. Interpretation 3 (1), SF21—SF30. https://doi.org/ 10.1190/INT-2014-0081.1.
- Dell, S., Walda, J., Hoelker, A., etal, 2020. Categorizing and correlating diffractivity attributes with seismic-reflection attributes using autoencoder networks. Geophysics 85 (4), O59–O70. https://doi.org/10.1190/geo2019-0574.1.
- Fomel, S., Landa, E., Taner, M.T., 2007. Poststack velocity analysis by separation and imaging of seismic diffractions. Geophysics 72 (6), U89–U94. https://doi.org/ 10.1190/1.2781533.
- Ford, J., Urgeles, R., Camerlenghi, A., et al., 2021. Seismic diffraction imaging to characterize mass-transport complexes: examples from the gulf of cadiz, south west iberian margin. J. Geophys. Res. Solid Earth 126 (3), 1–25. https://doi.org/ 10.1029/2020IB021474.
- Goyes-Peñafiel, P., Suárez-Rodríguez, L., Correa, C., et al., 2024. GAN supervised seismic data reconstruction: an enhanced learning for improved generalization. IEEE Trans. Geosci. Rem. Sens. 62, 1–10. https://doi.org/10.1109/TGRS.2024.3434474.
- He, K., Zhang, X., Ren, S., et al., 2016. Deep residual learning for image recognition. In: 2016 IEEE Conference on Computer Vision and Pattern Recognition (CVPR), pp. 770–778. https://doi.org/10.1109/CVPR.2016.90.
- Hou, Q., Zhou, D., Feng, J., 2021. Coordinate attention for efficient mobile network design. In: 2021 IEEE/CVF Conference on Computer Vision and Pattern Recognition (CVPR), pp. 13708—13717. https://doi.org/10.1109/CVPR46437.2021.01350.
- Huang, G., Liu, Z., Van Der Maaten, L., et al., 2017. Densely connected convolutional networks. In: 2017 IEEE Conference on Computer Vision and Pattern Recognition (CVPR), pp. 226–2269. https://doi.org/10.1109/CVPR.2017.243.
- Ioffe, S., Szegedy, C., 2015. Batch normalization: accelerating deep network training by reducing internal covariate shift. In: International Conference on Machine Learning, pp. 448–456. https://doi.org/10.5555/3045118.3045167.
- Ishak, M.A., Islam, M.A., Shalaby, M.R., et al., 2018. The application of seismic attributes and wheeler transformations for the geomorphological interpretation of stratigraphic surfaces: a case study of the F3 block, Dutch offshore sector, North sea. Geosciences 8 (3), 79. https://doi.org/10.3390/geosciences8030079.
- Jiang, J., Yang, W., Ren, H., et al., 2022. Diffraction separation and imaging using an improved singular value decomposition method. Geosci. Rem. Sens. Lett. IEEE 19, 1–5. https://doi.org/10.1109/LGRS.2022.3168016.
- Ke, W., Chen, J., Jiao, J., et al., 2017. SRN: side-output residual network for object

- symmetry detection in the wild. In: 2017 IEEE Conference on Computer Vision and Pattern Recognition (CVPR), pp. 302–310. https://doi.org/10.1109/CVPR.2017.40.
- Keller, J.B., 1962. Geometrical theory of diffraction. J. Opt. Soc. Am. 52 (2), 116–130. https://doi.org/10.1364/JOSA.52.000116.
- Kim, S., Seol, S.J., Byun, J., et al., 2022. Extraction of diffractions from seismic data using convolutional U-net and transfer learning. Geophysics 87 (2), V117–V129. https://doi.org/10.1190/geo2020-0847.1.
- Klokov, A., Baina, R., Landa, E., et al., 2010. Diffraction Imaging for Fracture Detection: Synthetic Case Study. 2010 SEG Technical Program Expanded Abstracts, pp. 3354–3358. https://doi.org/10.1190/1.3513545.
- Klokov, A., Fomel, S., 2012. Separation and imaging of seismic diffractions using migrated dip-angle gathers. Geophysics 77 (6), S131–S143. https://doi.org/ 10.1190/geo2012-0017.1.
- Landa, E., Keydar, S., 1998. Seismic monitoring of diffraction images for detection of local heterogeneities. Geophysics 63 (3), 1093–1100. https://doi.org/10.1190/ 11444387
- Li, Y., Hou, J.G., Li, Y.Q., et al., 2016. Features and classified hierarchical modeling of carbonate fracture-cavity reservoirs. Petrol. Explor. Dev. 43 (4), 655–662. https://doi.org/10.1016/S1876-3804(16)30076-3.
- Li, C.J., Zhao, J.T., Peng, S.P., et al., 2020. Separating and imaging diffractions of seismic waves in the full-azimuth dip-angle domain. J. Geophys. Eng. 17 (2), 339–356. https://doi.org/10.1093/jge/gxz110.
- Li, C.J., Zhao, J.T., Peng, S.P., et al., 2021. Prestack diffraction separation in the common virtual source gather. Geophysics 86 (2), S113—S124. https://doi.org/ 10.1190/geo2020-0105.1.
- Li, Z.C., Qu, Y.M., 2022. Research progress on seismic imaging technology. Pet. Sci. 19 (1), 128–146. https://doi.org/10.1016/j.petsci.2022.01.015.
- Li, Y., Huang, J., Lei, G., et al., 2023a. Plane-wave least-squares diffraction imaging using short-time singular spectrum analysis. J. Geophys. Eng. 20 (3), 453–473. https://doi.org/10.1093/jge/gxad021.
- Li, C.J., Peng, S.P., Cui, X.Q., et al., 2023b. 3-D pre-stack diffraction separation by extending the PWD method with parametrized local slope. Geophys. J. Int. 232 (2), 750–763. https://doi.org/10.1093/gji/ggac362.
- Li, X., Li, K., 2024. Fault-attri-attention: a method for fault identification based on seismic attributes attention. Neural Comput. Appl. 36, 3645–3661. https:// doi.org/10.1007/s00521-023-09265-7.
- Li, Z., Sun, H., Xu, R., et al., 2024a. Diffraction separation for the ground penetrating radar data by masking filters. Earth Sci. Res. J. 28 (2), 175–181. https://doi.org/10.15446/esrj.v28n2.112936.
- Li, C., Tian, L., Yao, Q., et al., 2024b. Least-squares diffraction imaging using variational mode decomposition. Geosci. Rem. Sens. Lett. IEEE 21, 1–5. https://doi.org/10.1109/LGRS.2024.3398649.
- Li, M., Yan, X., Hu, C., et al., 2024c. A self-supervised missing trace interpolation framework for seismic data reconstruction. Earth Science Informatics 17, 5991–6017. https://doi.org/10.1007/s12145-024-01485-2.
- Li, M., Huang, X., Tang, S., et al., 2025a. Reservoir-oriented migrated seismic image improvement and poststack seismic inversion using well-seismic mistie. Interpretation 13 (1), T99–T112. https://doi.org/10.1190/INT-2024-0008.1.
- Li, S., Li, Y., Shi, Y., et al., 2025b. Deep learning for seismic imaging in the presence of velocity errors. Geosci. Rem. Sens. Lett. IEEE 22, 1–5. https://doi.org/10.1109/LGRS.2024.3522250.
- Lin, P., Peng, S.P., Huang, X.G., et al., 2022a. Plane-wave destruction-based workflow for prestack diffraction separation in the shot domain. Pure Appl. Geophys. 179 (6), 2215–2229. https://doi.org/10.1007/s00024-022-03034-8.
- Lin, P., Peng, S.P., Li, C.J., et al., 2022b. Separation and imaging of seismic diffractions using geometric mode decomposition. Geophysics 88 (1), WA239–WA251. https://doi.org/10.1190/geo2022-0049.1.
- Lin, P., Peng, S.P., Xiang, Y., et al., 2023. Diffraction imaging of discontinuities using migrated dip-angle gathers. Geophysics 88 (1), V21–V32. https://doi.org/ 10.1190/geo2022-0100.1.
- Lin, P., Peng, S.P., Zhao, J.T., et al., 2020. Diffraction separation and imaging using multichannel singular-spectrum analysis. Geophysics 85 (1), V11–V24. https:// doi.org/10.1190/geo2019-0201.1.
- Lin, P., Zhao, J.T., Peng, S.P., 2021a. Low-rank diffraction separation using an improved MSSA algorithm. Acta Geophysica 69 (5), 1651–1665. https://doi.org/ 10.1007/s11600-021-00642-1.
- Lin, P., Zhao, J.T., Peng, S.P., et al., 2021b. A robust adaptive rank-reduction method for 3D diffraction separation and imaging. Pure Appl. Geophys. 178 (8), 2917–2931. https://doi.org/10.1007/s00024-021-02778-z.
- Liu, C., Ke, W., Jiao, J., et al., 2017. RSRN: rich side-output residual network for medial axis detection. In: 2017 IEEE International Conference on Computer Vision Workshops (ICCVW), pp. 1739–1743. https://doi.org/10.1109/ ICCVW.2017.204.
- Liu, L., Salim, H., Chen, K., et al., 2024. Adaptive merging migration. Geophysics 89 (4), S301–S310. https://doi.org/10.1190/geo2023-0158.1.
- Liu, Y.L., Lin, P., Peng, S.P., et al., 2025. Weighted multichannel singular spectrum analysis for diffraction amplitude preservation. Geophysics 90 (3), V191–V203. https://doi.org/10.1190/geo2024-0310.1.
- Lowney, B., Lokmer, I., O'Brien, G.S., et al., 2021a. Pre-migration diffraction separation using generative adversarial networks. Geophys. Prospect. 69 (5), 949–967. https://doi.org/10.1111/1365-2478.13086.
- Lowney, B., Lokmer, I., O'Brien, G.S., 2021b. Multi-domain diffraction identification: a supervised deep learning technique for seismic diffraction classification. Comput. Geosci. 155, 1–17. https://doi.org/10.1016/j.cageo.2021.104845.

- Markovic, M., Malehmir, R., Malehmir, A., 2023. Diffraction denoising using self-supervised learning. Geophys. Prospect. 71 (7), 1215–1225. https://doi.org/10.1111/1365-2478.13340.
- Markovic, M., Malehmir, R., Malehmir, A., 2022. Diffraction pattern recognition using deep semantic segmentation. Near Surf. Geophys. 20 (5), 507–518. https://doi.org/10.1002/nsg.12227.
- Park, J., Yoon, D., Seol, S.J., et al., 2019. Reconstruction of Seismic Field Data with Convolutional U-Net Considering the Optimal Training Input Data. 2019 SEG Technical Program Expanded Abstracts, pp. 4650–4654. https://doi.org/10.1190/segam2019-3216017.1.
- Perez, G., Marfurt, K.J., 2007. Improving lateral and vertical resolution of seismic images by correcting for wavelet stretch in common-angle migration. Geophysics 72 (6), C95–C104. https://doi.org/10.1190/1.2781619.
- Perez, G., Marfurt, K.J., 2008. New azimuthal binning for improved delineation of faults and fractures. Geophysics 73 (1), S7–S15. https://doi.org/10.1190/ 1.2813136.
- Protasov, M., Tcheverda, V., Shilikov, V., 2021. 3D diffraction imaging attributes and their application for fault and fracture localization and characterization. J. Appl. Geophys. 191, 1–9. https://doi.org/10.1016/j.jappgeo.2021.104346.
- Schleicher, J., Tygel, M., Hubral, P., 2007. Seismic True-Amplitude Imaging. Society of Exploration Geophysicists, Tulsa, Oklahoma, USA. https://doi.org/10.1190/ 1.9781560801672.
- Schneider, W.A., 1987. Integral formulation for migration in two and three dimensions. Geophysics 43 (1), 49–76. https://doi.org/10.1190/1.1440828.
- Serfaty, Y., Itan, L., Chase, D., et al., 2017. Wavefield Separation via Principle Component Analysis and Deep Learning in the Local Angle Domain. 2017 SEG Technical Program Expanded Abstracts, pp. 991–995. https://doi.org/10.1190/ segam2017-17676855.1.
- Sheng, T.J., Zhao, J.T., Peng, S.P., 2023. Seismic diffraction extraction method using Unet for weak signals. Chinese J. Geophys. 66 (3), 1192–1204. https://doi.org/10.6038/cjg2022Q0073 (in Chinese).
- Sheng, T.J., Zhao, J.T., Chen, Z.N., 2024. Diffraction imaging method using the pattern operator in migrated dip-angle gathers. Pure Appl. Geophys. 181, 3463–3484. https://doi.org/10.1007/s00024-024-03601-1.
- Sheng, T.J., Zhao, J.T., 2022. Separation and imaging of diffractions using a dilated convolutional neural network. Geophysics 87 (3), S117—S127. https://doi.org/10.1190/geo2021-0260.1.
- Smirnov, K., Landa, E., Fedyaev, I., 2021. New diffraction directivity prestack attributes for seismic fracture prediction. First Break 39 (2), 45–51. https://doi.org/10.3997/1365-2397.fb2021010.
- Sun, J.X., Yang, J.D., Li, Z.C., et al., 2022. Reflection and diffraction separation in the dip-angle common-image gathers using convolutional neural network. Geophysics 88 (1), WA281–WA291. https://doi.org/10.1190/geo2022-0157.1.
- Taner, M.T., Fomel, S., Landa, E., 2006. Separation and Imaging of Seismic Diffractions Using Plane-wave Decomposition. 2006 SEG Technical Program Expanded Abstracts, pp. 2401–2405. https://doi.org/10.1190/1.2370017.
- Tschannen, V., Ettrich, N., Delescluse, M., et al., 2020. Detection of point scatterers using diffraction imaging and deep learning. Geophys. Prospect. 68 (3), 830–844. https://doi.org/10.1111/1365-2478.12889.
- Üge, M.A., Kanlı, A.İ., 2024. Comparison of migration methods on seismic reflection data from the marmara sea and its interpretation using active tectonics. In: Recent Research on Geotechnical Engineering, Remote Sensing, Geophysics and Earthquake Seismology, pp. 313–316. https://doi.org/10.1007/978-3-031-

- 43218-7_73.
- Wang, H., Liu, X.Y., Chen, Y.K., 2020. Separation and imaging of seismic diffractions using a localized rank-reduction method with adaptively selected ranks. Geophysics 85 (6), V497–V506. https://doi.org/10.1190/geo2020-0215.1.
- Wang, J., Xiao, Z., Liu, C., et al., 2019. Deep learning for picking seismic arrival times.
 J. Geophys. Res. Solid Earth 124, 6612–6624. https://doi.org/10.1029/2019JB017536.
- Wang, T., Peng, S.P., Lin, P., et al., 2023. Diffraction enhancement using the double sparse dictionary method. Acta Geophysica 71 (3), 1259–1271. https://doi.org/10.1007/s11600-022-00981-7.
- Wang, X.Y., Chen, X., Yang, Z., et al., 2022. Research on diffraction wave reverse time migration imaging methods. Chinese J. Geophys. 65 (1), 320–332. https://doi.org/10.6038/cjg202100309 (in Chinese).
- Wei, H., Huang, W., Ji, T., et al., 2024. The method of seismic diffraction wave extraction based on PCA method and its application. Chem. Technol. Fuels Oils 59, 1313–1320. https://doi.org/10.1007/s10553-024-01647-4.
- Yang, N.X., Li, G.F., Li, T.H., et al., 2024. An improved deep dilated convolutional neural network for seismic facies interpretation. Pet. Sci. 21 (3), 1569–1583. https://doi.org/10.1016/j.petsci.2023.11.027.
- Yu, C., Wang, Y., Zhao, J., 2017. A seismic diffraction extraction method for the study of discontinuous geologies using a regularisation algorithm. Explor. Geophys. 48 (1), 49–55. https://doi.org/10.1071/EG15006.
- Yang, J., Peng, S.P., Zhao, J.T., 2023. Seismic diffraction attribute fusion for geological discontinuities in hot dry rock resources. Energies 16, 1138. https://doi.org/ 10.3390/en16031138.
- Zakarewicz, G., Maciel, S., Biloti, R., 2024a. DiffraPy: an open-source Python software for seismic diffraction imaging. Comput. Geosci. 186, 1–13. https://doi.org/10.1016/j.cageo.2024.105575.
- Zakarewicz, G., Maciel, S.T.R., Cunha, L.S., 2024b. Systematic literature review on seismic diffraction imaging. Earth Sci. Rev. 254, 1–27. https://doi.org/10.1016/ i.earscirey.2024.104792.
- Zhang, G.Y., Wang, Z.Z., Chen, Y.K., et al., 2018. Deep learning for seismic lithology prediction. Geophys. J. Int. 215 (2), 1368–1387. https://doi.org/10.1093/gji/ ggy344.
- Zhang, H., Li, Y., Huang, J., 2024. Conditional denoising diffusion probabilistic model for seismic diffraction separation and imaging. IEEE Trans. Geosci. Rem. Sens. 62, 1–13. https://doi.org/10.1109/TGRS.2024.3381193.
- Zhao, J.T., Sun, X.L., Peng, S.P., et al., 2019. Separating prestack diffractions with SVMF in the flattened shot domain. J. Geophys. Eng. 16 (2), 389–398. https://doi.org/10.1093/jge/gxz015.
- Zhao, J.T., Yu, C.X., Peng, S.P., et al., 2020. 3D diffraction imaging method using low-rank matrix decomposition. Geophysics 85 (1), S1–S10. https://doi.org/10.1190/geo2018-0417.1.
- Zhao, J.T., Yu, C.X., Peng, S.P., et al., 2021. Least-squares imaging of diffractions by solving a hybrid L1-L2 norm minimization problem. Geophysics 86 (1), S59–S72. https://doi.org/10.1190/geo2019-0720.1.
- Zhou, Y., 2024. Angle-domain common-image gathers for wave equation migration using regularized inversion. Acta Geophysica. https://doi.org/10.1007/s11600-024-01474-5.
- Znak, P., Gajewski, D., 2023. Identification and focusing of edge diffractions using wavefront attributes. Geophysics 88 (2), U31–U47. https://doi.org/10.1190/ geo2022-0071.1.